

## Molecular-Resolution Imaging of Ice Crystallized from Liquid Water

Jingshan S. Du<sup>1</sup>, Suvo Banik<sup>2,3</sup>, Henry Chan<sup>2</sup>, Birk Fritsch<sup>4</sup>, Ying Xia<sup>5</sup>, Ajay S. Karakoti<sup>1</sup>, Andreas Hutzler<sup>4</sup>, Subramanian K. R. S. Sankaranarayanan<sup>2,3</sup>, James J. De Yoreo<sup>1,5\*</sup>

<sup>1</sup>Physical Sciences Division, Pacific Northwest National Laboratory, Richland, WA 99352, United States

<sup>2</sup>Center for Nanoscale Materials, Argonne National Laboratory, Lemont, IL 60439, United States

<sup>3</sup>Department of Mechanical and Industrial Engineering, University of Illinois, Chicago, IL 60607, United States

<sup>4</sup>Helmholtz Institute Erlangen-Nürnberg for Renewable Energy (IEK-11), Forschungszentrum Jülich GmbH, 91058 Erlangen, Germany

<sup>5</sup>Department of Materials Science and Engineering, University of Washington, Seattle, WA 98195, United States

\*Correspondence should be addressed to james.deyoreo@pnl.gov (J.D.Y.)

### Abstract

Despite the ubiquity of ice, a molecular-resolution image of ice crystallized from liquid water or the resulting defect structure has never been obtained. Here, we report the stabilization and angstrom-resolution electron imaging of ice I<sub>h</sub> crystallized from liquid water by developing cryogenic liquid-cell transmission electron microscopy (CRYOLIC-TEM). We combine lattice mapping with molecular dynamics simulations to reveal that ice formation is highly tolerant to nanoscale defects such as misoriented subdomains and trapped gas bubbles, which are stabilized by molecular-scale structural motifs. Importantly, bubble surfaces adopt low-energy nanofacets and create negligible strain fields in the surrounding crystal. These bubbles can dynamically nucleate, grow, migrate, dissolve, and coalesce under electron irradiation and be monitored in situ near a steady state. This work opens the door to understanding water crystallization behaviors at an unprecedented spatial resolution.

## Main

Ice crystallization is one of the most important processes in the ecosphere and is central to atmospheric processes<sup>1-3</sup>, transportation safety<sup>4-7</sup>, biomedical cryopreservation<sup>8,9</sup>, and the food industry<sup>10,11</sup>. Among all ice species, hexagonal ice (type I<sub>h</sub>) crystallized from liquid water is most prevalent in the ambient. Due to the weak hydrogen bonds between water molecules, these structures can easily deform on the molecular scale during crystallization<sup>12,13</sup>. The precipitation of dissolved gas in water can further generate cavities in ice crystals; their formation and migration are exclusive to liquid-crystallized ice<sup>14,15</sup> with profound implications in glaciology and paleoclimatology<sup>16,17</sup>. Elucidating defects and microstructures of ice, particularly their molecular origins, is critical to understanding the thermodynamics, phase transformation, and mechanical properties of ice<sup>18</sup> and many other hydrogen-bonded crystals<sup>19-21</sup>.

Despite substantial interest in ice on the molecular scale, most studies rely on *in silico* simulations<sup>22-25</sup> and ensemble-scale spectroscopy and diffraction<sup>26-28</sup>. Meanwhile, real-space imaging in ice at this scale remains incredibly challenging due to the conflict between the low stability of ice and the harsh and invasive conditions often required by high-resolution imaging techniques. Recent breakthroughs in low-dose cryogenic transmission electron microscopy (cryo-TEM)<sup>29-32</sup> and ultra-high vacuum scanning probe microscopy<sup>33,34</sup> have enabled atomic-resolution imaging of ice condensed from the gas phase or converted from vitrified films. However, these experiments have typically been limited to crystals with random shapes and far-from-equilibrium structures because they rely on phase transformation and deposition at ultra-low temperatures in a high vacuum. Molecular-resolution imaging of the structures and defects formed by the crystallization of liquid water remains elusive to date.

Herein, we report an approach to freeze liquid water into high-quality ice I<sub>h</sub> samples, termed cryogenic liquid-cell TEM (CRYOLIC-TEM), which allows for high-resolution TEM (HRTEM) imaging. Inspired by advances in liquid-phase electron microscopy<sup>35</sup>, this method freezes liquid water between amorphous carbon (a-C) membranes into large-area (up to microns in size) single-crystalline ice I<sub>h</sub> films stable under the electron beam. Aberration-

corrected HRTEM imaging at a line resolution better than 2 Å is routinely achieved with a record of 1.3 Å in continuous single-crystalline regions. This new capability enables us to directly correlate lattice mapping with molecular dynamics (MD) simulations based on machine-learned models to elucidate defect nanostructures formed by liquid water crystallization. The formation, migration, coalescence, and dissolution trajectories of nanobubbles in single-crystalline ice are further observed in situ under the electron beam. This work provides a versatile way for accessing close-to-equilibrium ice  $I_h$  in TEM and unlocks previously inaccessible avenues to probe the nano- and molecular-scale interfacial configurations of ice and their structural dynamics.

### **Stabilizing high-quality ice $I_h$ single crystals from liquid water**

To freeze liquid water into ice  $I_h$  membranes suitable for TEM imaging, we first encapsulated deionized water between two TEM grids coated with a-C membranes and then loaded the sample onto a cryo-TEM sample holder (Fig. 1a). The sample was subsequently cooled by liquid nitrogen along with the holder. This process is substantially slower than vitrification in standard cryo-TEM, allowing for the crystallization of water. Flat, robust, and smooth a-C membranes are necessary for obtaining large-area, high-quality ice single crystals (Supplementary Fig. 1). The surface properties of the a-C membrane are similar to that of graphite (Supplementary Figs. 2 and 3). Exposing the cold sample to the atmosphere may result in the condensation of ice spherulites on the a-C film. This low-temperature (typically  $< -180$  °C) gas-phase ice deposition results in far-from-equilibrium mixtures of ice  $I_h$  and  $I_c$  (Supplementary Fig. 4), consistent with literature reports<sup>26,30,31,36</sup>. In contrast, ice formed by water crystallization between the a-C membranes often shows a flat morphology (Fig. 1b) and can be easily distinguished from condensed ice. In these crystals, single-crystalline regions aligned (or close) to the [0001] zone axis can often be found with areas up to several microns (Fig. 1c and Supplementary Fig. 5). The thickness of encapsulated ice can vary from  $\sim 10$  nm to micron-scale, depending on the geometry of the pocket. Still, high-quality HRTEM images can be acquired from relatively thin regions, achieving a record line resolution of 1.3 Å (Fig. 1d). Preparing samples on a double-tilt cryo holder further facilitates diffraction and HRTEM imaging of single crystals along other zone axes (Figs. 1e and f, and Supplementary Figs. 6 and 7).

Importantly, these single-crystalline areas can withstand HRTEM imaging for at least minutes (electron flux up to  $\sim 100 \text{ e } \text{\AA}^{-2} \text{ s}^{-1}$ ) without developing discernable nanoscale defects.

Cryogenic electron energy-loss spectroscopy (EELS) was performed to evaluate the high chemical purity of the encapsulated ice (Figs. 1g and h). After subtracting the inelastic scattering from the a-C membranes, the low-loss spectrum of encapsulated ice shows a relatively sharp peak centered at  $\sim 8.5 \text{ eV}$  and a broad peak at  $\sim 15 \text{ eV}$  (Fig. 1g). The former is characteristic of the excitonic  $1b_1 \rightarrow 4a_1$  orbital transition of  $\text{H}_2\text{O}$  in ice<sup>37,38</sup> and can be unequivocally distinguished from the  $\pi \rightarrow \pi^*$  transition from graphitic carbon<sup>38</sup> or aromatic organics<sup>37</sup> at lower energy. Accordingly, this method results in highly pure ice samples by avoiding the organic contamination frequently encountered by other encapsulation techniques, such as frozen graphene liquid cells<sup>39</sup>, caused by the solute concentration effect<sup>40,41</sup>. The broad peak is located at a lower energy than the bulk plasmon typically reported in the literature<sup>29,37,38</sup>, possibly due to the ice-carbon interface. Core-loss EELS profiles for the oxygen K edge also confirmed the highly pure chemical environment of the encapsulated ice (Fig. 1h).

### **Nanoscale subdomains at a defective crystal edge**

The strip-shaped crystal section in Fig. 1b appears to be a single crystal according to diffraction criteria (Fig. 1c). Surprisingly, lattice-resolved HRTEM images reveal highly defective textures near the edge areas despite a perfect hexagonal pattern in the Fourier transform (Figs. 2a and b). A relatively strong defocus was applied to obtain sufficient contrast. Indeed, these edge areas are substantially more volatile under beam irradiation (electron flux density  $< 20 \text{ e } \text{\AA}^{-2} \text{ s}^{-1}$ ) compared to large single-crystalline sections. The surface of this edge area is near-atomically smooth along the  $\langle \bar{1}100 \rangle$  direction, which suggests an exposed  $\{ \bar{2}110 \}$  surface assuming a vertical facet.

To analyze the spatial distribution of the nanoscale defects, we developed a lattice amplitude mapping approach to evaluate the local crystal misorientation from the zone axis (see Methods). In this map (Fig. 2c), a white color suggests that the local area's zone axis  $[0001]$  is perfectly aligned with the incident electrons. A red color, for

example, suggests that the local area is tilted by rotating around axis  $A$  in Fig. 2c. In this case, we only focus on the color balance rather than pixel intensities, as the varying thickness and the oscillatory contrast transfer function may complicate the latter. Nonetheless, nanostructures identified from lattice amplitude maps are generally insensitive to defocus, and only minor shifts in the overall color balance were observed at different defocus settings due to the slight imbalance of the beam deflectors (Supplementary Fig. 8). The lattice amplitude map at the defective edge reveals many subdomains on the 10- to 20-nm scale that are tilted away from each other despite the appearance of single-crystallinity according to the diffraction pattern (Fig. 1c) and the Fourier transform (Fig. 2b). This observation contrasts with the highly continuous lattices away from the thin edges (Supplementary Fig. 8).

By converting the red-green-blue (RGB) model of the composite image into the hue-saturation-intensity (HSI) model, we can further evaluate the orientation and the relative degree of the tilt (Fig. 2e). Here, the subdomain orientation (characterized by pixel hue) shows significantly wider distribution compared to that in continuous lattices (Supplementary Fig. 9). The two dominant orientations are  $\sim 9^\circ$  and  $\sim 127^\circ$ , suggesting that subdomain tilting towards the  $a$  axes (rotating around the normal vector of a primary prism plane) is slightly preferred. More importantly, the pixel saturation is associated with the relative tilt of the  $c$  axis from the imaging direction. The saturation histogram reveals that the tilt angle is distributed over a wide range with multiple broad peaks, indicating the presence of shallow local energy minima.

The HRTEM image further reveals the interfacial structures (Fig. 2d). Here, neighboring subdomains connect through relatively sharp interfaces or show gradual distortion over a few nanometers (i.e., mild change in the anisotropy of the lattice patterns). The typical tilt angle of such structures is on the scale of  $1^\circ$  to allow for the visibility of the ice  $\{\bar{1}100\}$  patterns according to both lattice visibility criteria<sup>42,43</sup> (Supplementary Fig. 13) and kinematical TEM simulations (Supplementary Figs. 14 to 25). Notably, a wide variety of interfaces exist with different tilt angles, orientations, and length scales.

MD simulations were employed to study the interfacial structure and energy landscape of these configurations. We used a coarse-grained machine-learned bond order potential (ML-BOP) model of water, which correctly captured the thermodynamic properties of water phases in good agreement with experiments<sup>23</sup>. A low-angle grain boundary (LAGB) between two single-crystalline domains was constructed by rotating one around the  $a_2$  axis, annealing at 260 K, and cooling to 93 K (see Methods and Supplementary Information). We systematically varied the sample thickness and initial tilt angle to evaluate the post-annealing structures and energetics in a broad structural space.

For very thin, freestanding ice structures consisting of a few molecular layers (thickness:  $\sim 4.4$  nm;  $t \leq 2$ , where  $t$  is the number of supercells (3 unit cells in the  $c$  axis,  $\sim 22$  Å)), the post-annealing tilt angle significantly deviates from the initial setup (Fig. 3a, upper panel). A wide range of tilt angles are unstable as structures bounce back or forward during annealing. As ice thickness increases, the range of unstable configurations and the tilt angle deviation during annealing are reduced. The same trend is also reflected in the energy landscape of the annealed structures (Fig. 3a, lower panel). A substantial energy variance was observed for few-layer structures, indicating their instability. However, for thicker films of  $t = 6$  and  $12$  (thickness:  $\sim 13.2$  and  $\sim 26.3$  nm), the energy profile converges and flattens out for tilt angles  $> \sim 0.5^\circ$  after an initial increase. This observation suggests that the energy penalties for varying the tilt angle of LAGBs in ice films may be minuscule.

To further understand the structural details of these boundaries, we examined the post-annealing MD trajectories ( $t = 6$ ; Fig. 3b). With a low tilt angle (case 1,  $0.34^\circ$ ), a defective region with disordered molecules and complex dislocations forms because the low tilt angle is insufficient to support a low-energy dislocation. This result corresponds to the initial energy rise as the tilt angle increases (Fig. 3a, lower panel). When the tilt angle is sufficiently large (case 3,  $1.70^\circ$ ), a perfect edge dislocation (Burgers vector,  $\mathbf{b} = \frac{1}{3}\langle 1\bar{2}10 \rangle$ ) forms to compensate for the lattice mismatch (Fig. 3b). Interestingly, a moderate tilt angle (case 2,  $0.96^\circ$ ) leads to a mixed edge and screw dislocation, with the Burgers vector roughly pointing to the  $a_3$  axis. If we look along the  $a_2$  axis, i.e., roughly

along the dislocation line (Fig. 3c), the crystal in case 2 only has a sufficient tilt angle to accommodate a visual half-plane mismatch, in contrast to the one-unit-cell mismatch in case 3. To avoid the unstable partial edge dislocation, a partial screw dislocation was also generated, leading to a perfect unit cell mismatch (Fig. 3d and Supplementary Fig. 29). This behavior is repeatedly seen in crystals with a larger thickness and when more than one dislocation line is present (Supplementary Fig. 30).

Based on the analyses above, we summarize how ice films develop LAGBs while minimizing the energy penalty (Fig. 3e). In conventional materials, such as bulk metals (upper schematic), the LAGB energy increases monotonously against the tilt angle with increasing dislocation density<sup>44</sup>. A large tilt angle gap exists in few-layer freestanding ice structures due to the unstable configuration (middle schematic). In ice films  $> \sim 10$  nm relevant to our TEM experiments (lower schematic), the energy of the LAGB first increases due to elastic strain and the formation of disordered structures but then quickly flattens out over a wide range of tilt angles, owing to the formation of perfect dislocations regardless of the tilt angle. The presence of unstable configurations and shallow local energy minima could further explain the mild preference for certain tilt angles observed in the experiment (Fig. 2e, lower panel). As such, LAGBs with various tilt angles can co-exist in ice films with low energy penalties.

This conclusion is consistent with our TEM results. The annealed configuration from the MD (case 3) was used for multislice TEM simulation (Fig. 3f and g). The simulated TEM image correctly reproduced the isotropic hexagonal lattices on the right that are perfectly aligned with the [0001] zone axis. Meanwhile, the pattern on the left is elongated in the horizontal direction due to tilting, consistent with the lattice anisotropy observed from experimental images in tilted subdomains (Fig. 2d). The increase in anisotropy is also evidenced by the horizontal intensity profile for a row of lattice spots in Fig. 3g. Importantly, even though a single dislocation line is present in the middle, the pattern anisotropy exhibits a gradual transition across 1 to 2 nm, consistent with the interfacial transition observed in the experiments.

## Trapped gas bubbles

Away from the defective edges described above, we investigated the interior regions of single-crystalline ice. Continuous hexagonal lattices were observed over large areas (Fig. 4a to c), and the lattice amplitude map reveals an absence of subdomains (Fig. 4d).

In this region, we discovered many trapped gas bubbles in the form of nanoscale cavities in the crystal (Fig. 4a, circular and elliptical features labeled by arrows). Thickness gradients due to bubble curvature are evidenced by the significant contrast variations near the bubble surfaces. The formation of nanosized trapped bubbles is attributed to the relatively fast cooling rate of the thin sample compared to bulk freezing<sup>45</sup>.

By calculating the in-plane lattice distortion tensors using geometric phase analysis (GPA)<sup>46</sup>, we found that almost no additional strain field exists in the crystals surrounding the nanobubbles (Figs. 4e to g and Supplementary Fig. 12). The distribution of all in-plane lattice distortion indicators (strains, rotation, and dilation) is significantly narrower than that of the subdomain-containing defective edge (Fig. 4h).

Previous MD simulations for metals, such as Al, predicted strain fields surrounding a nanocavity ( $r = 10$  nm) on the scale of 1%–3%<sup>47</sup>. To understand the absence of such a strain field in ice, we first used continuum theories of elasticity to estimate the strain distribution around a spherical cavity<sup>48</sup>. The maximum elastic strains caused by the Laplace pressure of an ice nanobubble ( $r = 10$  nm) is  $< 0.4\%$  (Supplementary Fig. 35). As such, nanobubbles in ice should be expected to cause negligible strain fields, which agrees with the HRTEM-derived strain maps.

Our MD simulations also confirm this conclusion. We modeled a spherical cavity ( $r = 6$  nm) in an ice single crystal, melted the structures within 3 nm in the vicinity of the cavity surface, and recrystallized them in silico (see Methods). Volumetric strain analysis shows no discernable strain accumulation around the cavity, with a mean and standard deviation of only 0.30% and 1.00% (Fig. 4j).



To further investigate the inner surface structure of the bubbles on the molecular scale, we moved to single-crystalline ice regions with a much lower thickness, where bubbles became quasi-cylindrical through-holes (Fig. 4i and Supplementary Movie 1). The reduced thickness allowed direct imaging and recognition of the lattice structures near the bubble surface. Notably, despite the overall curved shape, most exposed surfaces on the molecular scale can be attributed either to the primary prism planes,  $\{\bar{1}100\}$ , or secondary prism planes,  $\{\bar{2}110\}$ , assuming vertical facets. These two surfaces are the lowest-energy facets in ice  $I_h$  perpendicular to  $[0001]$ <sup>49,50</sup>. The ratio between the projected length of the primary and secondary prism planes is circa 3.8:1 (Table 1).

The bubble model in MD simulations was also used to reveal the surface faceting at the molecular level (see Supplementary Information). A significant fraction of the surface molecules are exposed as basal, primary prism, or secondary prism planes (Fig. 4k and Table 1). The fractional ratio between the primary and secondary prism planes in the MD-simulated cross-section at the center (Supplementary Fig. 33) and HRTEM follow the same trend predicted by their surface energy (Table 1). This result indicates that the trapped gas bubbles in the experiments are very close to thermodynamic equilibrium, and the nanoscale configurations we observed could reflect those in sufficiently annealed bubbles. We note that a lower amount of basal planes were observed in MD than prism planes despite their lower surface energy because the former must fit into the top and bottom curvatures. As such, trapped bubbles in ice are defined both by the macroscopic rounded shape and molecular-scale facets to minimize the total surface energy. The presence of these nanofacets may be important in defining the stability and migration kinetics of trapped gas bubbles in glacial systems<sup>16,51</sup>.

### **In situ observation of dynamic bubble trajectories**

When we elevated the stage temperature to  $-70$  °C and reduced the electron flux density to  $25 \text{ e } \text{Å}^{-2} \text{ s}^{-1}$ , we observed nucleation and growth of new nanobubbles in single-crystalline ice sections under HRTEM conditions (Fig. 5a and Supplementary Movie 2). The newly generated bubbles show similar shapes with trapped nanobubbles imaged at about  $-180$  °C. Furthermore, these bubbles can migrate in the crystal and completely

dissolve under the same conditions (Fig. 5b and Supplementary Movie 3) while the ice sample stays single-crystalline, suggesting that the system is near a steady state for bubble generation and ice recrystallization.

Bubbles can also dynamically coalesce and merge into larger ones (Fig. 5c and Supplementary Movie 4). In this observation, two bubbles approached each other, and their outlines initially showed different thickness contrasts. However, the contrast matched upon coalescence, which suggests that the two bubbles physically connected rather than passed by at different vertical positions. The ice surfaces in the bubbles are highly dynamic, as shown by the significant reshaping of the merging ones.

The persistent hexagonal patterns in the Fourier transform of the movies suggest that the ice sample stayed single-crystalline in these observations. GPA was performed on all frames to evaluate the mechanical consequences of the bubble trajectories. Here, the mean value of in-plane lattice dilation reflects the global distortion of the sample and only fluctuated within a range of  $\sim 1\%$  throughout the experiments (Fig. 5d). The standard deviation of the lattice dilation was further calculated to evaluate local lattice distortion (Fig. 5e). Indeed, most data fall between the levels observed in the defective edges (Fig. 2) and the bubble-containing interior sections (Fig. 4) at about  $-180\text{ }^\circ\text{C}$ . These observations further show that nanobubbles cause insignificant strain fields in ice crystals even during their dynamic evolution.

Bubble formation in ice under the electron beam can mainly be attributed to radiolysis<sup>52</sup> and knock-on damage by the incident electrons<sup>53</sup>. To evaluate the radiolytic chemistry under the experimental conditions, we extended approaches developed for water radiolysis in liquid-phase electron microscopy<sup>54,55</sup> to lower temperatures and numerically calculated the reaction kinetics at  $-70\text{ }^\circ\text{C}$  and  $25\text{ e } \text{\AA}^{-2}\text{ s}^{-1}$  (see Methods). Notably, the system reaches a steady state within seconds of gas generation (Fig. 5f), consistent with in situ TEM results. The formation of substantial  $\text{H}_2$  and  $\text{O}_2$  species is in agreement with cryogenic EELS analyses of amorphous ice<sup>56,57</sup>, highlighting the potential role of these gas molecules in constituting bubble volumes in our experiments.

## Discussion

We have presented the first molecular-resolution imaging of nanoscopic defects in ice  $I_h$  crystallized from liquid water. The new sample preparation method, which successfully crystallized liquid water into thin ice films between a-C membranes, was a critical factor that led to this imaging breakthrough. These samples contain large-area single-crystalline regions that are sufficiently stable under HRTEM conditions for extended imaging. Despite the presence of a heterogeneous interface between ice/water and the encapsulating membrane, the ice sample thickness is typically well beyond the thickness of interfacial regions (on the order of 1 nm)<sup>58</sup> such that there is no significant deviation from the physics of bulk phase transformation. By maneuvering the sample temperature and electron flux density, a near-steady state of bubble generation and dissolution in crystalline ice was achieved. A finer control over the imaging conditions will likely pave the way to the direct imaging of ice-water interfacial structures and, moreover, crystallization and melting dynamics with molecular resolution, a holy grail in the ice research community<sup>59-61</sup>. Experimental images and movies can now be directly compared and correlated to computations on an unprecedented molecular length scale to reveal the underlying structures, molecular interactions, and phase transformation pathways. The direct extraction of such angstrom-scale information provides a new research paradigm for theory, modeling, and forecasting of ice crystallization and melting in environmental, biological, and material systems.

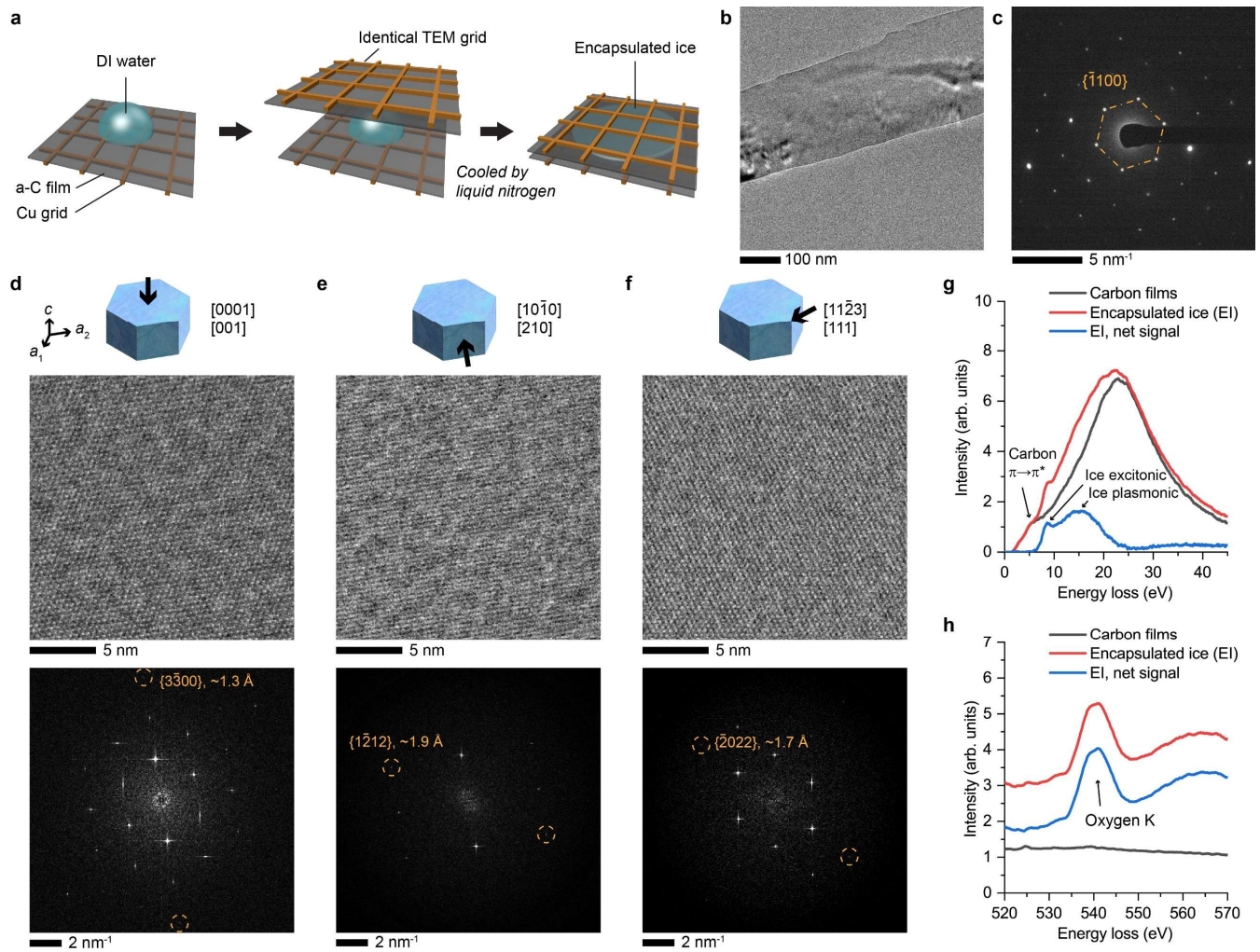


**Fig. 1: Crystallization of liquid water for HRTEM.** **a**, Schematic of encapsulating ice crystal sections from deionized (DI) water between amorphous carbon (a-C) films. **b**, TEM image of a thin strip of ice crystal encapsulated between a-C films. **c**, SAED pattern showing overall single crystallinity along the [0001] zone axis. **d–f**, Schematic of the viewing direction (top row), average background subtraction (ABS)-filtered HRTEM (middle row), and Fourier transform (bottom row) of ice  $I_h$  along three zone axes. Both Miller-Bravais and Miller indices were given for convenience. **g,h**, EELS profiles in the low-loss (**g**) and oxygen K core-loss (**h**) regions. The low-loss profiles were deconvolved using the Fourier-log algorithm to remove the zero-loss peak and plural scattering.

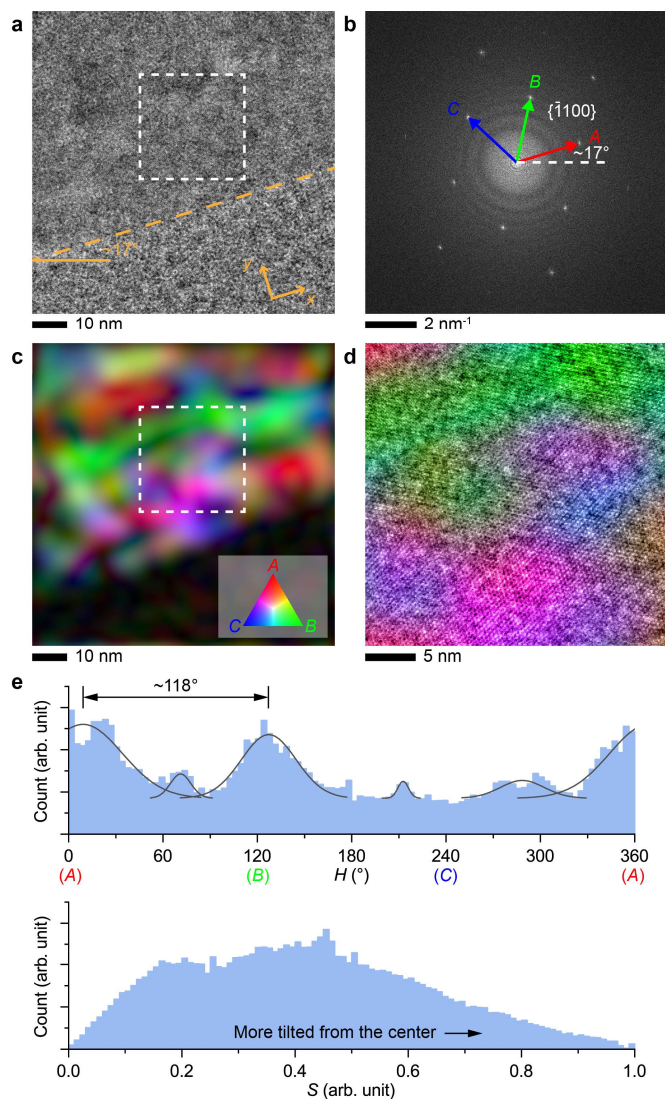


**Fig. 2: Nanoscale subdomain configuration at a defective crystal edge.** **a**, HRTEM image of a defective ice section near the crystal edge (orange dashed line is a visual guideline). **b**, Fourier transform of image a with three pairs of  $\{1100\}$  reflections labeled as *A*, *B*, and *C*. **c**, Intensity map of the three reflections in **b** indexed by red, green, and blue colors. **d**, ABS-filtered HRTEM from the area highlighted by the dashed box in **a** colored by **c**. **e**, Histograms of pixel hue (upper) and saturation (lower) in the ice area in **c** in the hue-saturation-intensity (HSI) model. Curves in the upper panel are Gaussian fitting results.

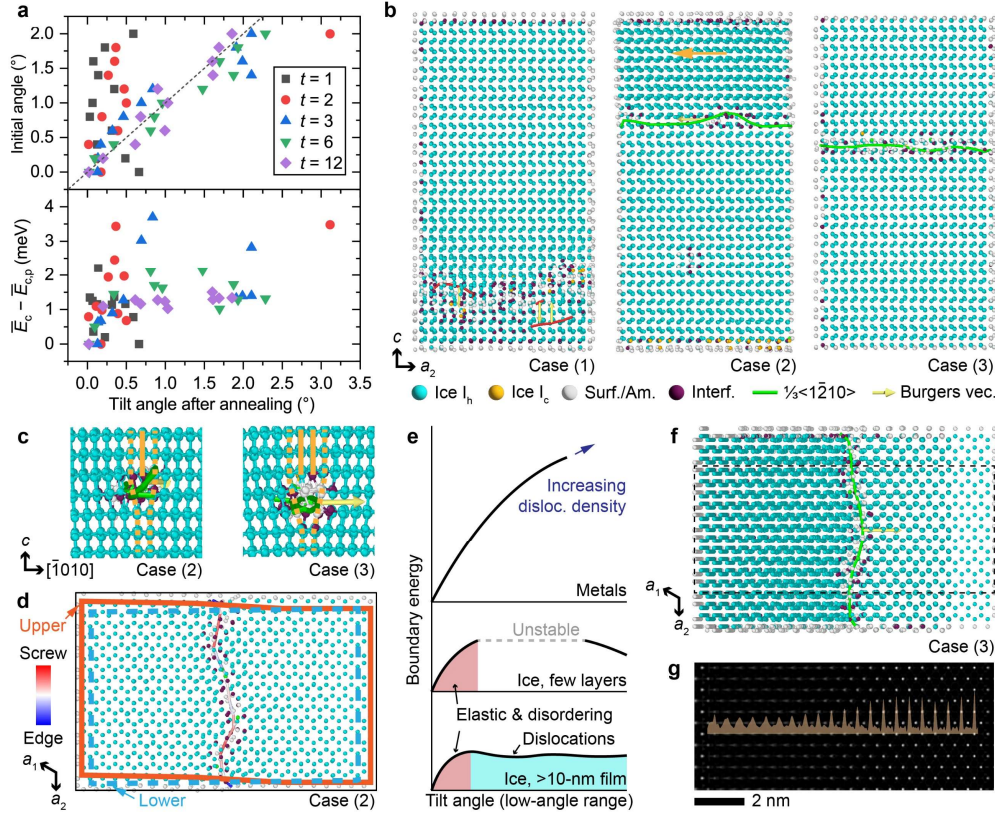


**Fig. 3: Molecular dynamics studies of low-angle grain boundaries in ice films.** **a**, The initial angle (upper panel) and the mean cohesive energy per molecule of annealed MD models at 93 K ( $\bar{E}_c$ ) compared to that of an annealed perfect crystal ( $\bar{E}_{c,p}$ ; lower panel) as a function of the final tilt angle. Crystal thickness ( $t$ ) is expressed in the number of supercells (3 unit cells in the  $c$  axis,  $\sim 22$  Å). **b**, Cross-sectional models of the tilted ice ( $t = 6$ ) with a final tilt angle of  $0.34^\circ$  (1),  $0.96^\circ$  (2), and  $1.70^\circ$  (3). **c**, Cross-sectional models of the dislocation core of cases (2) and (3). **d**, Cross-sectional model of case (2) showing molecules on the slip plane, the configuration of upper and lower domains, and the local character of the dislocation. **e**, Schematic energy diagrams of low-angle grain boundaries in typical metals, freestanding few-layer ice, and thicker ice films  $> 10$  nm. **f,g**, Top-down view of the case (3) with cross-section exposing the dislocation core (**f**) and multislice-simulated TEM image of the crystal in the dashed-box area (**g**). Defocus:  $-55$  nm. The orange trace in (**g**) is the intensity profile of a row of lattice patterns. All structural models share a legend below panel **b**. Beads: water molecules in ice, surface/amorphous (surf./am.), interfacial (interf.), or hydrate-like local configurations (other colors). Red curves represent dislocations of other types.

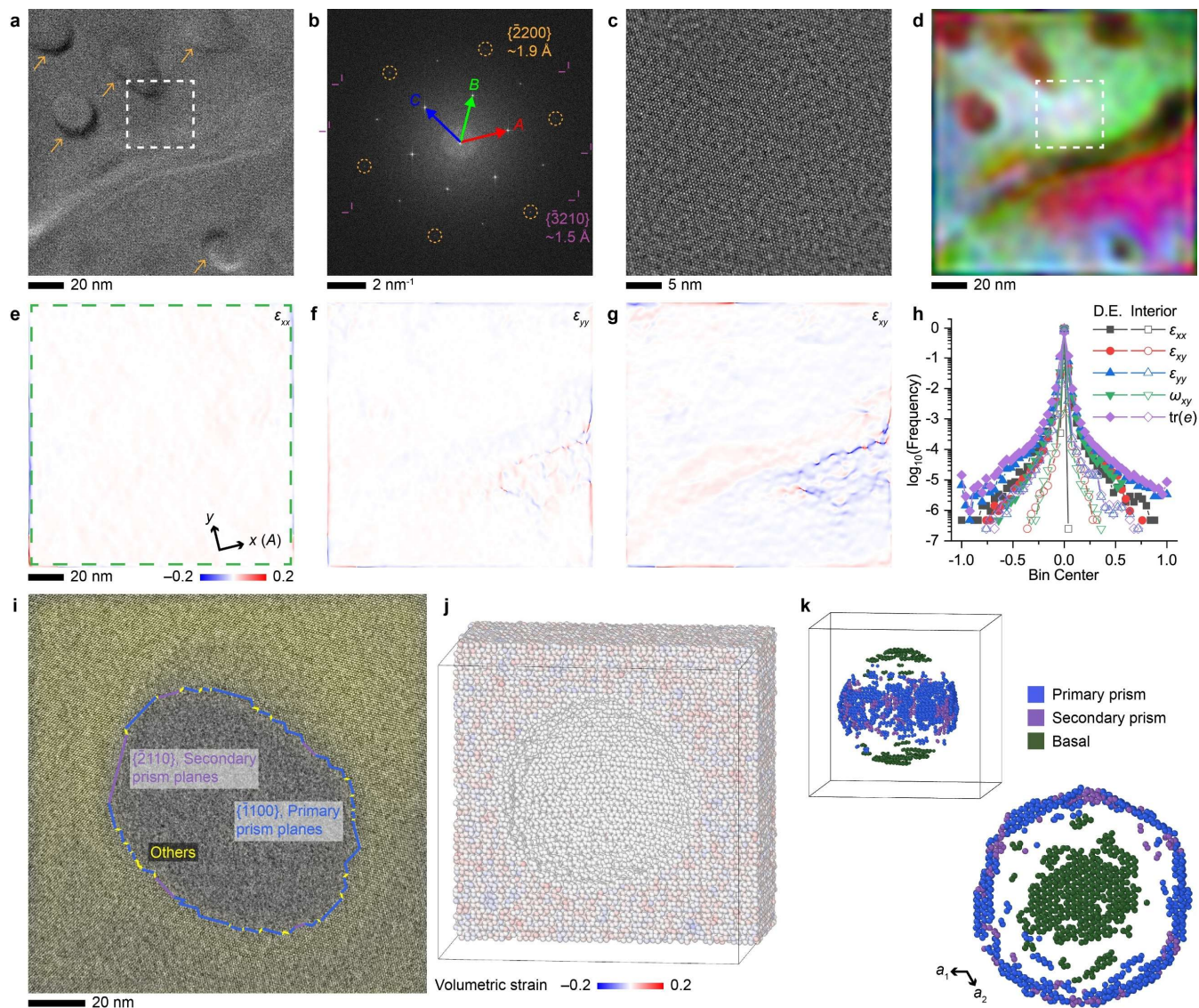


**Fig. 4: Trapped gas nanobubbles formed by water crystallization.** **a**, HRTEM image of an ice  $I_h$  crystal aligned to the  $[0001]$  zone axis from the interior area of a crystal section. Arrows indicate trapped gas bubbles. **b**, Fourier transform of **a**. **c**, ABS-filtered HRTEM image from the area highlighted by the dashed box in **a**. **d**, Intensity map of the three reflections in **b** indexed by red, green, and blue colors. **e–g**, In-plane strain distribution from GPA for  $xx$  (**e**),  $yy$  (**f**), and  $xy$  (**g**). **h**, Histogram of mechanical quantities in this area (Interior) and the defective edge (D.E.; Fig. 2a). **i**, ABS-filtered HRTEM image of a through-hole in thin ice films. The exposed crystal plane assignment assumes vertical facets with a projected length of at least 3 unit cells. A yellow shade indicates areas showing ice lattices. **j**, Cross-sectional view of an MD-simulated nanobubble ( $r = 6$  nm) in ice color-coded by the local volumetric strain. **k**, Surface beads from the nanobubble color-coded by recognized facets in 3D and top-down views.

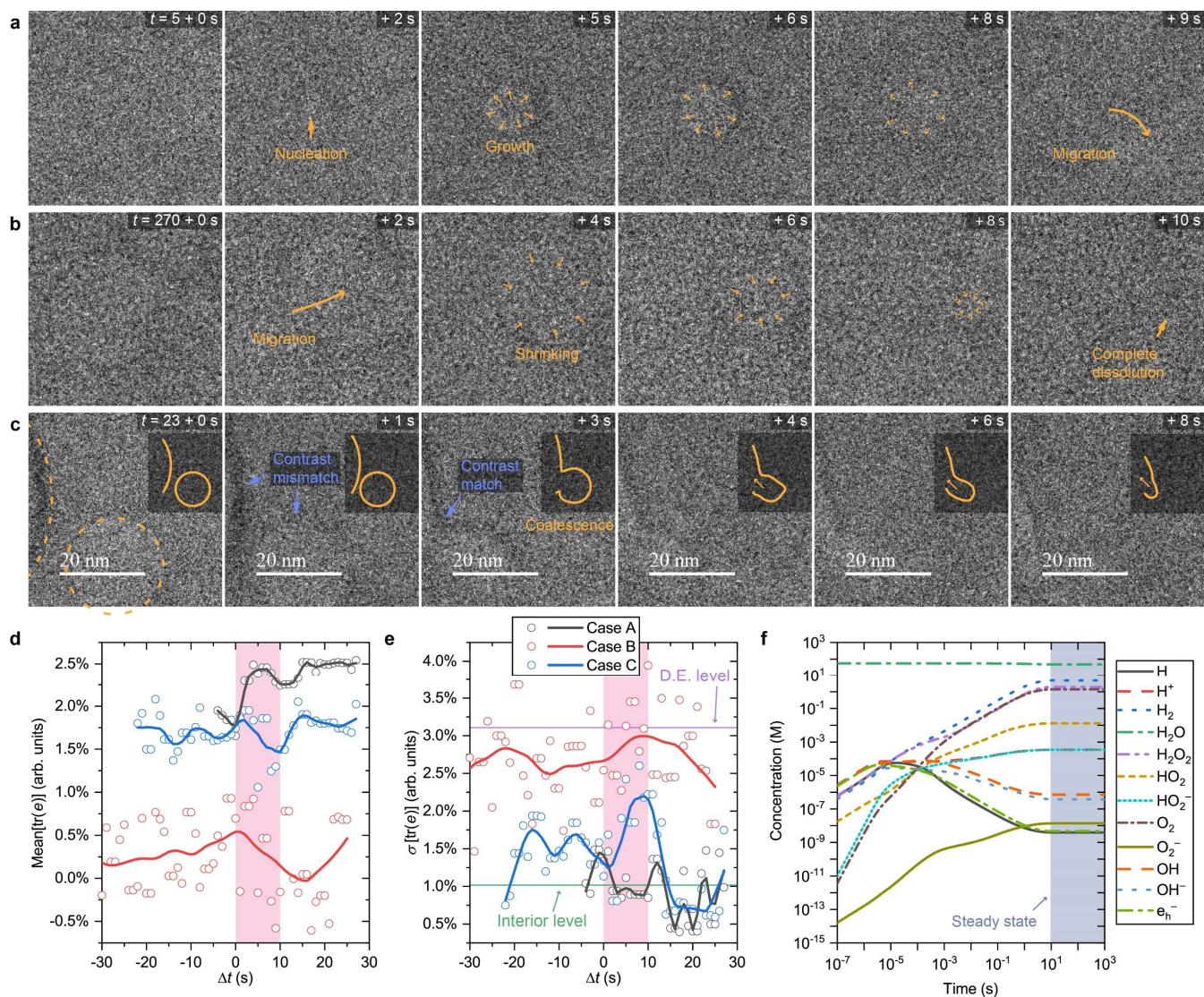


**Fig. 5: Direct observation of gas bubble trajectories in single-crystalline ice  $I_h$  near a steady state.** **a–c,** Time-sequence drift-corrected HRTEM images at a stage temperature of  $-70$  °C and an electron flux density of  $25 \text{ e } \text{\AA}^{-2} \text{ s}^{-1}$  showing three types of bubble dynamics: nucleation and growth (**a**), dissolution (**b**), and coalescence (**c**). Insets in **c**: solid curves represent the shape evolution of the bubble outlines (dashed curves in the first panel). All images share the scale bars shown in **c**. **d,e,** The mean (**d**) and standard deviation (**e**) of lattice dilation  $[tr(e)]$  as a function of time from three HRTEM sequences [**a** to **c**; Movies S2 to S4]. Pink shades indicate the period shown in panels **a** to **c**. Curves are smoothing results (LOWESS, span = 0.15). D.E.: defective edge. **f,** Calculated ice radiolysis kinetics at  $-70$  °C and an electron flux density of  $25 \text{ e } \text{\AA}^{-2} \text{ s}^{-1}$ .



**Table 1: Molecular-scale facet composition on nanobubble surfaces.** Percentages represent length fractions measured from HRTEM along [0001] and molecular coverages from MD. \*Ratio between primary and secondary prism planes. \*\*Cross-section (thickness = 5 nm) of the bubble center perpendicular to [0001]. \*\*\*Excess free surface energy of the facet at 0 K calculated from MD.

| Method                          | Basal | Primary prism | Secondary prism | Other | PP/SP ratio * |
|---------------------------------|-------|---------------|-----------------|-------|---------------|
| HRTEM (2D)                      | –     | 68.8%         | 17.9%           | 13.3% | 3.84          |
| MD (3D)                         | 8.21% | 18.5%         | 4.68%           | 68.6% | 3.95          |
| MD cross-section**              | –     | 40.8%         | 10.3%           | 48.9% | 3.96          |
| Energy (meV/Å <sup>2</sup> )*** | 6.48  | 6.78          | 7.82            | –     | –             |

## References

- Murray, B. J., O'Sullivan, D., Atkinson, J. D. & Webb, M. E. Ice nucleation by particles immersed in supercooled cloud droplets. *Chem. Soc. Rev.* **41**, 6519-6554, (2012).
- Hoose, C. & Möhler, O. Heterogeneous ice nucleation on atmospheric aerosols: a review of results from laboratory experiments. *Atmos. Chem. Phys.* **12**, 9817-9854, (2012).
- Gottelman, A., Liu, X., Barahona, D., Lohmann, U. & Chen, C. Climate impacts of ice nucleation. *J. Geophys. Res. Atmos.* **117**, (2012).
- Lynch, F. T. & Khodadoust, A. Effects of ice accretions on aircraft aerodynamics. *Prog. Aerosp. Sci.* **37**, 669-767, (2001).
- Hill, E. in *44th AIAA Aerospace Sciences Meeting and Exhibit* Ch. 81, (American Institute of Aeronautics and Astronautics, 2006).
- Masterson, D. M. State of the art of ice bearing capacity and ice construction. *Cold Reg. Sci. Technol.* **58**, 99-112, (2009).
- Mintu, S. & Molyneux, D. Ice accretion for ships and offshore structures. Part 1 - State of the art review. *Ocean Eng.* **258**, 111501, (2022).
- Murray, K. A. & Gibson, M. I. Chemical approaches to cryopreservation. *Nat. Rev. Chem.* **6**, 579-593, (2022).
- John Morris, G. & Acton, E. Controlled ice nucleation in cryopreservation – A review. *Cryobiology* **66**, 85-92, (2013).
- Erickson, M. C. & Hung, Y. C. *Quality in Frozen Food*. (Springer US, 2012).
- Sun, L., Zhu, Z. & Sun, D.-W. Regulating ice formation for enhancing frozen food quality: Materials, mechanisms and challenges. *Trends Food Sci. Technol.* **139**, 104116, (2023).
- Libbrecht, K. G. The physics of snow crystals. *Rep. Prog. Phys.* **68**, 855-895, (2005).
- Bartels-Rausch, T. *et al.* Ice structures, patterns, and processes: A view across the icefields. *Rev. Mod. Phys.* **84**, 885-944, (2012).
- Carte, A. E. Air Bubbles in Ice. *Proc. Phys. Soc.* **77**, 757, (1961).
- Shao, K., Song, M., Zhang, X. & Zhang, L. Growth and distribution characteristics of trapped air bubbles in ice slices. *Phys. Fluids* **35**, (2023).
- Wengrove, M. E., Pettit, E. C., Nash, J. D., Jackson, R. H. & Skillingstad, E. D. Melting of glacier ice enhanced by bursting air bubbles. *Nat. Geosci.* **16**, 871-876, (2023).
- Bender, M., Sowers, T. & Brook, E. Gases in ice cores. *Proc. Nat. Acad. Sci.* **94**, 8343-8349, (1997).
- de Koning, M. Crystal imperfections in ice Ih. *J. Chem. Phys.* **153**, 110902, (2020).
- Głowacki, E. D., Irimia-Vladu, M., Bauer, S. & Sariciftci, N. S. Hydrogen-bonds in molecular solids – from biological systems to organic electronics. *J. Mater. Chem. B* **1**, 3742-3753, (2013).
- Sloan, E. D. Clathrate Hydrates: The Other Common Solid Water Phase. *Ind. Eng. Chem. Res.* **39**, 3123-3129, (2000).

- 21 Li, P., Ryder, M. R. & Stoddart, J. F. Hydrogen-Bonded Organic Frameworks: A Rising Class of Porous Molecular Materials. *Acc. Mater. Res.* **1**, 77-87, (2020).
- 22 Johnston, J. C. & Molinero, V. Crystallization, Melting, and Structure of Water Nanoparticles at Atmospherically Relevant Temperatures. *J. Am. Chem. Soc.* **134**, 6650-6659, (2012).
- 23 Chan, H. *et al.* Machine learning coarse grained models for water. *Nat. Commun.* **10**, 379, (2019).
- 24 Davies, M. B., Fitzner, M. & Michaelides, A. Accurate prediction of ice nucleation from room temperature water. *Proc. Nat. Acad. Sci.* **119**, e2205347119, (2022).
- 25 Kapil, V. *et al.* The first-principles phase diagram of monolayer nanoconfined water. *Nature* **609**, 512-516, (2022).
- 26 Kuhs, W. F., Sippel, C., Falenty, A. & Hansen, T. C. Extent and relevance of stacking disorder in "ice I<sub>c</sub>". *Proc. Nat. Acad. Sci.* **109**, 21259-21264, (2012).
- 27 del Rosso, L. *et al.* Cubic ice I<sub>c</sub> without stacking defects obtained from ice XVII. *Nat. Mater.* **19**, 663-668, (2020).
- 28 Rosu-Finsen, A. *et al.* Medium-density amorphous ice. *Science* **379**, 474-478, (2023).
- 29 Kobayashi, K., Koshino, M. & Suenaga, K. Atomically Resolved Images of I<sub>h</sub> Ice Single Crystals in the Solid Phase. *Phys. Rev. Lett.* **106**, 206101, (2011).
- 30 Huang, X. *et al.* Tracking cubic ice at molecular resolution. *Nature* **617**, 86-91, (2023).
- 31 Lin, Y. *et al.* Surface premelting of ice far below the triple point. *Proc. Nat. Acad. Sci.* **120**, e2304148120, (2023).
- 32 Lee, M. *et al.* Observing growth and interfacial dynamics of nanocrystalline ice in thin amorphous ice films. *Nat. Commun.* **15**, 908, (2024).
- 33 Ma, R. *et al.* Atomic imaging of the edge structure and growth of a two-dimensional hexagonal ice. *Nature* **577**, 60-63, (2020).
- 34 Hong, J. *et al.* Imaging surface structure and premelting of ice I<sub>h</sub> with atomic resolution. *Nature* **630**, 375-380, (2024).
- 35 Sung, J. *et al.* Liquid-Phase Transmission Electron Microscopy for Reliable In Situ Imaging of Nanomaterials. *Annu. Rev. Chem. Biomol. Eng.* **13**, 167-191, (2022).
- 36 Thürmer, K. & Nie, S. Formation of hexagonal and cubic ice during low-temperature growth. *Proc. Nat. Acad. Sci.* **110**, 11757-11762, (2013).
- 37 Sun, S., Shi, S. & Leapman, R. Water distributions of hydrated biological specimens by valence electron energy loss spectroscopy. *Ultramicroscopy* **50**, 127-139, (1993).
- 38 Daio, T. *et al.* In-Situ ESEM and EELS Observation of Water Uptake and Ice Formation in Multilayer Graphene Oxide. *Sci. Rep.* **5**, 11807, (2015).
- 39 Ghodsi, S. M., Anand, S., Shahbazian-Yassar, R., Shokuhfar, T. & Megaridis, C. M. In Situ Study of Molecular Structure of Water and Ice Entrapped in Graphene Nanovessels. *ACS Nano* **13**, 4677-4685, (2019).
- 40 Park, J. *et al.* Graphene Liquid Cell Electron Microscopy: Progress, Applications, and Perspectives. *ACS Nano* **15**, 288-308, (2021).
- 41 Crook, M. F. *et al.* EELS Studies of Cerium Electrolyte Reveal Substantial Solute Concentration Effects in Graphene Liquid Cells. *J. Am. Chem. Soc.* **145**, 6648-6657, (2023).
- 42 Fraundorf, P., Qin, W., Moeck, P. & Mandell, E. Making sense of nanocrystal lattice fringes. *J. Appl. Phys.* **98**, 114308, (2005).
- 43 Du, J. S. *et al.* Multistage Transformation and Lattice Fluctuation at AgCl-Ag Interface. *J. Phys. Chem. Lett.* **8**, 5853-5860, (2017).
- 44 Zhang, L., Gu, Y. & Xiang, Y. Energy of low angle grain boundaries based on continuum dislocation structure. *Acta Mater.* **126**, 11-24, (2017).
- 45 Qi, J. *et al.* Evolution of Bulk Nanobubbles under Different Freezing Conditions. *Langmuir* **39**, 16873-16880, (2023).
- 46 Hÿtch, M. J., Snoeck, E. & Kilaas, R. Quantitative measurement of displacement and strain fields from HREM micrographs. *Ultramicroscopy* **74**, 131-146, (1998).
- 47 Pizzagalli, L. & David, M.-L. Surface stress calculations for nanoparticles and cavities in aluminum, silicon, and iron: influence of pressure and validity of the Young-Laplace equation. *Materials Theory* **5**, 5, (2021).

- 48 Landau, L. D., Lifshitz, E. M., Kosevich, A. M. & Pitaevskii, L. P. in *Theory of Elasticity* Vol. 7 *Course of Theoretical Physics* Ch. 1, 1-37 (Butterworth-Heinemann, 1986).
- 49 Shultz, M. J., Bisson, P. J. & Brumberg, A. Best Face Forward: Crystal-Face Competition at the Ice–Water Interface. *J. Phys. Chem. B* **118**, 7972-7980, (2014).
- 50 Shultz, M. J. Ice Surfaces. *Annu. Rev. Phys. Chem.* **68**, 285-304, (2017).
- 51 Dadic, R., Light, B. & Warren, S. G. Migration of air bubbles in ice under a temperature gradient, with application to “Snowball Earth”. *J. Geophys. Res. Atmos.* **115**, D18125, (2010).
- 52 Falls, A. H., Wellinghoff, S. T., Talmon, Y. & Thomas, E. L. A transmission electron microscopy study of hexagonal ice. *J. Mater. Sci.* **18**, 2752-2764, (1983).
- 53 Unwin, P. N. T. & Muguruma, J. Electron microscope observations on the defect structure of ice. *Phys. Status Solidi A* **14**, 207-216, (1972).
- 54 Schneider, N. M. *et al.* Electron–Water Interactions and Implications for Liquid Cell Electron Microscopy. *J. Phys. Chem. C* **118**, 22373-22382, (2014).
- 55 Fritsch, B. *et al.* Radiolysis-Driven Evolution of Gold Nanostructures – Model Verification by Scale Bridging In Situ Liquid-Phase Transmission Electron Microscopy and X-Ray Diffraction. *Adv. Sci.* **9**, 2202803, (2022).
- 56 Leapman, R. D. & Sun, S. Cryo-electron energy loss spectroscopy: observations on vitrified hydrated specimens and radiation damage. *Ultramicroscopy* **59**, 71-79, (1995).
- 57 Abellan, P., Gautron, E. & LaVerne, J. A. Radiolysis of Thin Water Ice in Electron Microscopy. *J. Phys. Chem. C* **127**, 15336-15345, (2023).
- 58 Garcia, R. Interfacial Liquid Water on Graphite, Graphene, and 2D Materials. *ACS Nano*, (2022).
- 59 Bai, G., Gao, D., Liu, Z., Zhou, X. & Wang, J. Probing the critical nucleus size for ice formation with graphene oxide nanosheets. *Nature* **576**, 437-441, (2019).
- 60 Moberg, D. R. *et al.* The end of ice I. *Proc. Nat. Acad. Sci.* **116**, 24413-24419, (2019).
- 61 Piaggi, P. M., Weis, J., Panagiotopoulos, A. Z., Debenedetti, P. G. & Car, R. Homogeneous ice nucleation in an ab initio machine-learning model of water. *Proc. Nat. Acad. Sci.* **119**, e2207294119, (2022).

## **Methods**

### ***Materials and chemicals***

Deionized (DI) water was generated by an ELGA PURELAB flex 2 system with a resistivity of 18.2 M $\Omega$ ·cm.

Carbon-coated Cu grids for transmission electron microscopy (TEM) were purchased from Ted Pella, Inc.

Ammonium persulfate ( $\geq 98\%$ ) was purchased from Sigma-Aldrich.

### ***Preparation of encapsulated ice $I_h$ samples***

In a typical experiment, 1–3  $\mu\text{L}$  of DI water was dispensed on the carbon side of a TEM grid and loaded on a Gatan 626 single-tilt or a 915 double-tilt liquid nitrogen cryo-transfer holder, with the carbon/water side facing up. Another identical grid was put on top of the first one, with the carbon side facing down. The grid orientation was roughly aligned when placing the second grid, and the surface tension of water would then align and adhere the grids together. Depending on the models of the TEM and their column vacuum level, the sample can either be frozen inside or outside the column with liquid nitrogen. Freezing outside the TEM in the cryo transfer station is typically preferred for consistency. In either case, the copper shield remains closed during sample freezing.

### ***Cryogenic transmission electron microscopy (cryo-TEM) and data processing***

TEM was performed on an FEI Titan Environmental TEM [extreme-brightness Schottky field-emission gun (X-FEG), 300 kV] equipped with a CEOS double-hexapole aberration corrector (CETCOR) for the image-forming lenses and a Gatan UltraScan 1000 charge-coupled device (CCD) scintillation camera. TEM along zone axes other than [0001] was performed on an FEI ThemIS TEM (X-FEG, 300 kV) equipped with a CEOS CETCOR for the image-forming lenses and an FEI Ceta 16M complementary metal-oxide-semiconductor (CMOS) scintillation camera. Electron energy-loss spectroscopy (EELS) was performed on a JEOL JEM-ARM300CF GRAND ARM (cold FEG, 300 kV) equipped with a JEOL dodecapole expanding trajectory aberration corrector for the probe-forming lenses and a Gatan Imaging Filter (GIF) Quantum system. Convergence angle: 41.2 mrad; EELS collection angle: 62.4 mrad. During the experiments, the temperature readout from the cryo holder is typically between  $-180$  and  $-178$  °C.

Average background subtraction (ABS) filtering<sup>62</sup> of high-resolution TEM (HRTEM) images was performed using a script in Gatan DigitalMicrograph ([http://www.dmscripting.com/hrtem\\_filter.html](http://www.dmscripting.com/hrtem_filter.html)) with the following parameters: Delta = 5.0%, BW n = 4, BW Ro = 0.8, and low-frequency tapering = 1.0%. Low-loss EELS profiles were first processed by removing the plural scattering using the Fourier-log algorithm. All EELS profiles were smoothed by adjacent averaging with a 50-pixel moving window size.

### ***Calculation of lattice maps from electron images***

The lattice amplitude maps were calculated with the following procedures: (1) obtain the Fourier transform image; (2) mask only the circular areas containing the desired pair of lattice reflections and assign zero to all other pixels (mask diameter =  $0.2 \text{ nm}^{-1}$ ); (3) perform inverse Fourier transformation; (4) obtain the absolute value of the image (i.e., flip the sign of negative intensity values); (5) perform Gaussian smoothing with  $\sigma = 5$  pixels (this may vary depending on the pixel size); (6) repeat this process for the other two pair of reflections; (7) overlay the three resulting images as a red/green/blue (RGB) stack. The lattice distortion maps (strain, rotation, and dilation) were calculated using the Strain++ package (<https://jjppeters.github.io/Strainpp/>) based on the geometric phase analysis (GPA) algorithm<sup>46</sup>. Zero-distortion points in GPA were chosen at the maximum-modulus frequencies in the Fourier transform. The Gaussian mask size ( $3\sigma$ ) is set to 1/8 of the  $\{\bar{1}100\}$   $g$  vector length.

### ***In situ cryogenic electron microscopy***

After obtaining an ice sample in TEM, the holder temperature was raised to  $-70 \text{ }^\circ\text{C}$  and stabilized. Movies were recorded by screen capturing at an electron flux density of  $25 \text{ e } \text{Å}^{-2} \text{ s}^{-1}$  determined on the fluorescence screen through the integrated sensor. Frames were registered using the ImageJ StackReg module (<http://bigwww.epfl.ch/thevenaz/stackreg/>).

### ***Characterization of the carbon membranes***

The thickness and surface roughness of the carbon membranes from the TEM grids were measured based on a previously described method<sup>63</sup>. Briefly, the copper grid was etched by an ammonium persulfate aqueous solution

( $\sim 100 \text{ mg mL}^{-1}$ ), leaving the carbon membrane floating on the solution surface. The carbon membrane was then transferred to a glass slide and then to DI water for cleaning, which was repeated two times. Finally, the membrane was transferred to a silicon wafer ready for atomic force microscopy (AFM) imaging. AFM was performed on an Asylum Research Cypher ES with a Bruker RFESPA-75 probe (resonance frequency, 75 kHz; spring constant,  $3 \text{ N m}^{-1}$ ). The scan rate was 1.5 Hz, and the amplitude was between 300 and 350 mV. The thickness was determined at the edge of the membrane ruptures caused by drying. Image processing and quantification were performed with the Gwyddion package<sup>64</sup> (<http://gwyddion.net/>).

The chemical characteristics of the carbon membrane surface were studied by X-ray photoelectron spectroscopy (XPS) on a Kratos Axis Ultra that uses a monochromatic focused Al  $K\alpha$  X-ray (1486.7 eV) source. The instrument was calibrated prior to the introduction of the sample and referenced to binding energies for Cu 2p<sub>3/2</sub> at  $932.67 \pm 0.05 \text{ eV}$  and Au 4f at  $84.0 \pm 0.05 \text{ eV}$ . The base pressure of the sample analysis chamber was maintained at  $1.6 \times 10^{-9} \text{ Torr}$ . The sample was prepared by adhering the carbon-coated copper grid to a stainless-steel bar using copper tape. The tape was used only in the corners while at least two data points were analyzed from the center of the grid. Since the carbon-coated copper grid was conductive, no neutralizer was applied, and the results were analyzed without any charge correction.

Furthermore, the water contact angle was measured by drop-casting  $\sim 1\text{-}\mu\text{L}$  of DI water onto a TEM grid and immediately capturing a side-view image. The drop shape was fitted to calculate the contact angle<sup>65</sup>. Experiments were repeated on three separate TEM grids.

### ***Simulation of electron microscopy and diffraction***

Kinematical HRTEM simulation from single crystals was performed using the ReciPro package<sup>66</sup> (<https://seto77.github.io/ReciPro/>). The simulation assumes a parallel beam condition, a beam energy of  $300 \text{ keV} \pm 0.8 \text{ eV}$ ,  $C_s = 4 \text{ }\mu\text{m}$ , and  $C_c = 1.4 \text{ mm}$ . Selected area electron diffraction (SAED) patterns were simulated based on the dynamical theory using ReciPro, assuming a sample thickness of 30 nm. Polycrystal SAED radial profiles

were simulated based on the kinematical theory using the CrystalDiffract package (CrystalMaker Software, <https://crystalmaker.com/crystaldiffract/>). These simulations used the experimentally derived ice I<sub>h</sub> crystal structure in the space group  $P6_3/mmc$ <sup>67,68</sup>.

Multislice TEM simulation<sup>69</sup> based on explicit models from coarse-grained molecular dynamics (MD) was performed with the QSTEM package<sup>70</sup> ([https://www.physik.hu-berlin.de/en/sem/software/software\\_qstem](https://www.physik.hu-berlin.de/en/sem/software/software_qstem)) using the same TEM parameters. An F atom was used instead of a water molecule in the coarse-grained MD model for image simulation.

### ***Coarse-grained molecular dynamics simulations***

The MD simulations were performed using a coarse-grained machine-learned bond order potential (ML-BOP) model of water<sup>23</sup>. For grain boundary simulations, minimal-energy configurations of bi-grain ice models with different thicknesses and tilt angles were first established with the conjugate gradient algorithm<sup>71</sup>. The models were subsequently annealed in silico in the LAMMPS package<sup>72</sup> at 260 K and then gradually cooled to 93 K in the microcanonical ( $NVE$ ) ensemble. For nanobubble simulations, a cavity of a radius of 6 nm was created in a single-crystalline ice I<sub>h</sub> model by removing the molecules within. The model was first equilibrated in LAMMPS at 260 K and 1 bar. The surface areas of the bubble (thickness: 3 nm) were subsequently heated to 270 K and then 370 K for melting, and finally cooled back to 260 K for recrystallization. See Supplementary Information for detailed procedures.

The OVITO package<sup>73</sup> (<https://www.ovito.org/>) was used to perform local symmetry identification using the CHILL+ algorithm<sup>74</sup> and dislocation analysis using an extended dislocation extraction algorithm (DXA)<sup>75</sup>.

### ***Numerical calculation of radiolysis kinetics***

Radiation chemistry is modeled by considering the interplay of twelve reactants relevant for liquid-phase TEM ( $H_2O$ ,  $H_2$ ,  $O_2$ ,  $H_2O_2$ ,  $H$ ,  $OH$ ,  $HO_2$ ,  $H^+$ ,  $HO_2^-$ ,  $O_2^-$ ,  $OH^-$ , and the solvated electron  $e_{h^-}$ ). An amorphous ice sample

with no spatial anisotropy is considered. The reactions among these reactants span a kinetic model that is described by a set of coupled differential equations<sup>76</sup>:

$$\frac{\partial c_i}{\partial t} = \sum_j k_j \left( \prod_l c_l \right) - \sum_{m \neq j} k_m \left( \prod_n c_n \right) + \rho \psi G_i.$$

**Eq. 1**

Here,  $c_i$  denotes the concentration of the reactant  $i$ ,  $t$  the time,  $k$  the reaction-rate constant of the respective reaction,  $G_i$  the generation value ( $G$ -value) of  $i$  upon electron irradiation, and  $\rho$  the density of amorphous ice ( $0.92 \text{ g L}^{-1}$ )<sup>77</sup>. The dose rate  $\psi$  is calculated from<sup>78</sup>:

$$\psi = \frac{S}{e} \phi.$$

**Eq. 2**

In this equation,  $\phi$  is the electron flux density, and  $e$  is the elementary charge. As the inelastic scattering of 300 keV electrons in amorphous ice appears to be reasonably close to that in water<sup>79,80</sup>, a density-normalized stopping power  $S$  of  $2.36 \text{ MeV cm}^{-2} \text{ g}^{-1}$  was approximated<sup>81</sup>. For an electron-flux density of  $25 \text{ e \AA}^{-2} \text{ s}^{-1}$ , this yields a dose rate of  $9.45 \times 10^7 \text{ Gy s}^{-1}$ .

The harnessed kinetic model extrapolates Arrhenius-based rate constants<sup>82</sup> to lower temperatures (Supplementary Table 8). As cryogenic  $G$ -values are unavailable<sup>57</sup>, room temperature values are used (Supplementary Table 9)<sup>83</sup>. Modeling is performed using a temperature-dependent extension of AuRaCh<sup>55</sup>. The code is available at <https://github.com/BirkFritsch/Radiolysis-simulations>.

## References

- 23 Chan, H. *et al.* Machine learning coarse grained models for water. *Nat. Commun.* **10**, 379, (2019).
- 46 Hýtch, M. J., Snoeck, E. & Kilaas, R. Quantitative measurement of displacement and strain fields from HREM micrographs. *Ultramicroscopy* **74**, 131-146, (1998).
- 55 Fritsch, B. *et al.* Radiolysis-Driven Evolution of Gold Nanostructures – Model Verification by Scale Bridging In Situ Liquid-Phase Transmission Electron Microscopy and X-Ray Diffraction. *Adv. Sci.* **9**, 2202803, (2022).
- 57 Abellan, P., Gautron, E. & LaVerne, J. A. Radiolysis of Thin Water Ice in Electron Microscopy. *J. Phys. Chem. C* **127**, 15336-15345, (2023).
- 62 Kilaas, R. Optimal and near-optimal filters in high-resolution electron microscopy. *J. Microsc.* **190**, 45-51, (1998).



- 63 Du, J. S. *et al.* Windowless Observation of Evaporation-Induced Coarsening of Au-Pt Nanoparticles in Polymer Nanoreactors. *J. Am. Chem. Soc.* **140**, 7213-7221, (2018).
- 64 Nečas, D. & Klapetek, P. Gwyddion: an open-source software for SPM data analysis. *Cent. Eur. J. Phys.* **10**, 181-188, (2012).
- 65 Stalder, A. F. *et al.* Low-bond axisymmetric drop shape analysis for surface tension and contact angle measurements of sessile drops. *Colloids Surf. A* **364**, 72-81, (2010).
- 66 Seto, Y. & Ohtsuka, M. ReciPro: free and open-source multipurpose crystallographic software integrating a crystal model database and viewer, diffraction and microscopy simulators, and diffraction data analysis tools. *J. Appl. Crystallogr.* **55**, 397-410, (2022).
- 67 Goto, A., Hondoh, T. & Mae, S. The electron density distribution in ice Ih determined by single - crystal x - ray diffractometry. *J. Chem. Phys.* **93**, 1412-1417, (1990).
- 68 Fortes, A. D. *et al.* No evidence for large-scale proton ordering in Antarctic ice from powder neutron diffraction. *J. Chem. Phys.* **120**, 11376-11379, (2004).
- 69 Kirkland, E. J. *Advanced Computing in Electron Microscopy*. 2nd edn, (Springer, 2010).
- 70 Koch, C. T. *Determination of core structure periodicity and point defect density along dislocations*, Arizona State University, (2002).
- 71 Shewchuk, J. R. An introduction to the conjugate gradient method without the agonizing pain. (Carnegie Mellon University, 1994).
- 72 Thompson, A. P. *et al.* LAMMPS-a flexible simulation tool for particle-based materials modeling at the atomic, meso, and continuum scales. *Comput. Phys. Commun.* **271**, 108171, (2022).
- 73 Stukowski, A. Visualization and analysis of atomistic simulation data with OVITO—the Open Visualization Tool. *Modell. Simul. Mater. Sci. Eng.* **18**, 015012, (2010).
- 74 Nguyen, A. H. & Molinero, V. Identification of Clathrate Hydrates, Hexagonal Ice, Cubic Ice, and Liquid Water in Simulations: the CHILL+ Algorithm. *J. Phys. Chem. B* **119**, 9369-9376, (2015).
- 75 Stukowski, A., Bulatov, V. V. & Arsenlis, A. Automated identification and indexing of dislocations in crystal interfaces. *Modell. Simul. Mater. Sci. Eng.* **20**, 085007, (2012).
- 76 Fritsch, B., Malgaretti, P., Harting, J., Mayrhofer, K. J. J. & Hutzler, A. Precision of Radiation Chemistry Networks: Playing Jenga with Kinetic Models for Liquid-Phase Electron Microscopy. *Precis. Chem.* **1**, 592-601, (2023).
- 77 Langmore, J. P. & Smith, M. F. Quantitative energy-filtered electron microscopy of biological molecules in ice. *Ultramicroscopy* **46**, 349-373, (1992).
- 78 Fritsch, B. *et al.* Accessing local electron-beam induced temperature changes during in situ liquid-phase transmission electron microscopy. *Nanoscale Adv.* **3**, 2466-2474, (2021).
- 79 Yesibolati, M. N. *et al.* Electron inelastic mean free path in water. *Nanoscale* **12**, 20649-20657, (2020).
- 80 Pimblott, S. M., LaVerne, J. A., Mozumder, A. & Green, N. J. B. Structure of electron tracks in water. 1. Distribution of energy deposition events. *J. Phys. Chem.* **94**, 488-495, (1990).
- 81 Berger, M. J., Coursey, J. S., Zucker, M. A. & Chang, J. Stopping-Power and Range Tables for Electrons, Protons, and Helium Ions. (National Institute of Standards and Technology, Gaithersburg, MD, 1998).
- 82 Ambrožič, B. *et al.* Controlling the radical-induced redox chemistry inside a liquid-cell TEM. *Chem. Sci.* **10**, 8735-8743, (2019).
- 83 Pastina, B. & LaVerne, J. A. Effect of Molecular Hydrogen on Hydrogen Peroxide in Water Radiolysis. *J. Phys. Chem. A* **105**, 9316-9322, (2001).

## Acknowledgments

We thank L. Kovarik, D. Li, and M. Zhang of Pacific Northwest National Laboratory (PNNL) and K. Bustillo, R. Dhall, and J. Ciston of Lawrence Berkeley National Laboratory (LBNL) for their helpful discussions. We thank J. J. P. Peters (Trinity College Dublin) for implementing stack processing in the Strain++ package. Microscopy and

analysis were supported by the U.S. Department of Energy (DOE) Office of Science (SC) Basic Energy Sciences (BES) Division of Materials Science and Engineering, Synthesis and Processing Sciences program (FWP 67554) at PNNL. Molecular dynamics simulations were supported by the Data, Artificial Intelligence, and Machine Learning at Scientific User Facilities program under the Digital Twin Project at Argonne National Laboratory. Development of ice encapsulation and imaging methodology was supported by a U.S. DOE SC Distinguished Scientist Fellows award (FWP 77246) at PNNL. A portion of this research was performed on project awards (60286, 60620, and 60789) from the Environmental Molecular Sciences Laboratory at PNNL. Work at the Molecular Foundry and the National Energy Research Scientific Computing Center was supported by the U.S. DOE SC BES under Contract No. DE-AC02-05CH11231. Work at the Center for Nanoscale Materials was supported by the U.S. DOE SC BES under Contract No. DE-AC02-06CH11357. J.S.D. acknowledges a Washington Research Foundation Postdoctoral Fellowship. PNNL is a multiprogram national laboratory operated for the DOE by Battelle under Contract DE-AC05-76RL01830.

### **Author Contributions**

J.S.D. and J.D.Y. conceived and designed the study. J.S.D. performed electron microscopy and its simulations. H.C. and S.K.R.S.S. developed the machine-learned coarse-grained model for water. S.B. and H.C. performed molecular dynamics simulations. B.F. and A.H. performed radiolysis calculations. Y.X., A.S.K., and J.S.D. characterized the membrane surface. J.D.Y., S.K.R.S.S., and A.H. supervised the study. J.S.D. led manuscript drafting. All authors analyzed and discussed the data and revised the manuscript.

### **Competing Interests**

The authors declare no competing interests.

## Supplementary Information

### Molecular-Resolution Imaging of Ice Crystallized from Liquid Water

Jingshan S. Du<sup>1</sup>, Suvo Banik<sup>2,3</sup>, Henry Chan<sup>2</sup>, Birk Fritsch<sup>4</sup>, Ying Xia<sup>5</sup>, Ajay S. Karakoti<sup>1</sup>, Andreas Hutzler<sup>4</sup>, Subramanian K. R. S. Sankaranarayanan<sup>2,3</sup>, James J. De Yoreo<sup>1,5\*</sup>

<sup>1</sup>Physical Sciences Division, Pacific Northwest National Laboratory, Richland, WA 99352, United States

<sup>2</sup>Center for Nanoscale Materials, Argonne National Laboratory, Lemont, IL 60439, United States

<sup>3</sup>Department of Mechanical and Industrial Engineering, University of Illinois, Chicago, IL 60607, United States

<sup>4</sup>Helmholtz Institute Erlangen-Nürnberg for Renewable Energy (IEK-11), Forschungszentrum Jülich GmbH, 91058 Erlangen, Germany

<sup>5</sup>Department of Materials Science and Engineering, University of Washington, Seattle, WA 98195, United States

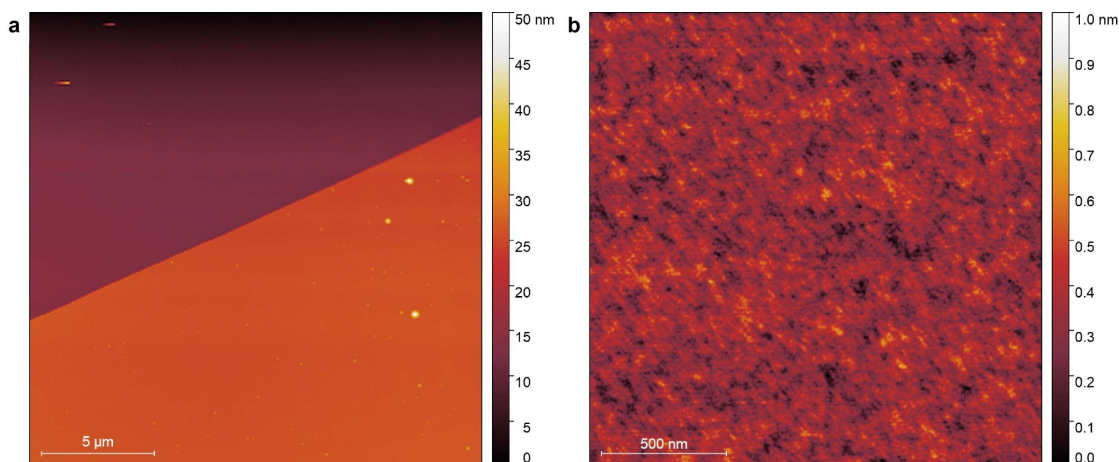
\*Correspondence should be addressed to [james.deyoreo@pnnl.gov](mailto:james.deyoreo@pnnl.gov) (J.D.Y.)

#### **This PDF file contains:**

- Supplementary Microscopy and Characterization Results
- Supplementary Details for Molecular Dynamics Simulation
- Supplementary Details for Theoretical Calculations
- Supplementary Tables 1–9
- Supplementary Figures 1–37
- Captions for Supplementary Movies 1–4
- Captions for Supplementary Data 1–3
- References

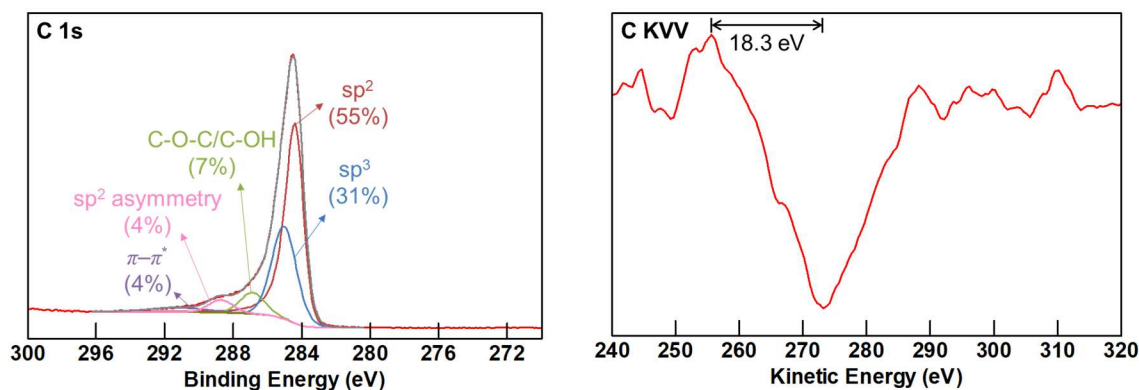
## Supplementary Microscopy and Characterization Results

### Carbon membrane characteristics



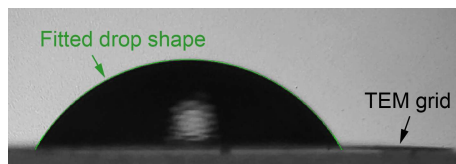
**Supplementary Fig. 1. Characterization of the amorphous carbon membrane used in this study by AFM. a**, Height image of a broken edge of the thin film for thickness determination: terrace-fitted step height = 12.0 nm. **b**, Height image of the film surface for roughness measurement: RMS roughness  $S_q = 83.4$  pm and mean roughness  $S_a = 66.3$  pm.

We studied the surface chemical characteristics of the carbon membrane using X-ray photoelectron spectroscopy (XPS), as shown in Supplementary Fig. 2. The C 1s core level spectrum was deconvoluted to assess the relative contributions of various carbon environments. The peak deconvolution showed contributions from carbon in both  $sp^2$  and  $sp^3$  environments from the amorphous carbon. The  $sp^2$  carbon contribution was found to be 55% which agrees with the  $D$  parameter value assessed from the C KVV Auger emission<sup>1</sup>. In addition to the hydrocarbon, a peak corresponding to C-O at 286.8 eV was also present and its relative concentration of 7% matches well with the 6.3% oxygen present in the overall sample. The other two peaks were assigned to the  $\pi-\pi^*$  shake-up structure at 291.2 eV, while a secondary peak was fitted to account for the asymmetry in the  $sp^2$  carbon 1s peak.



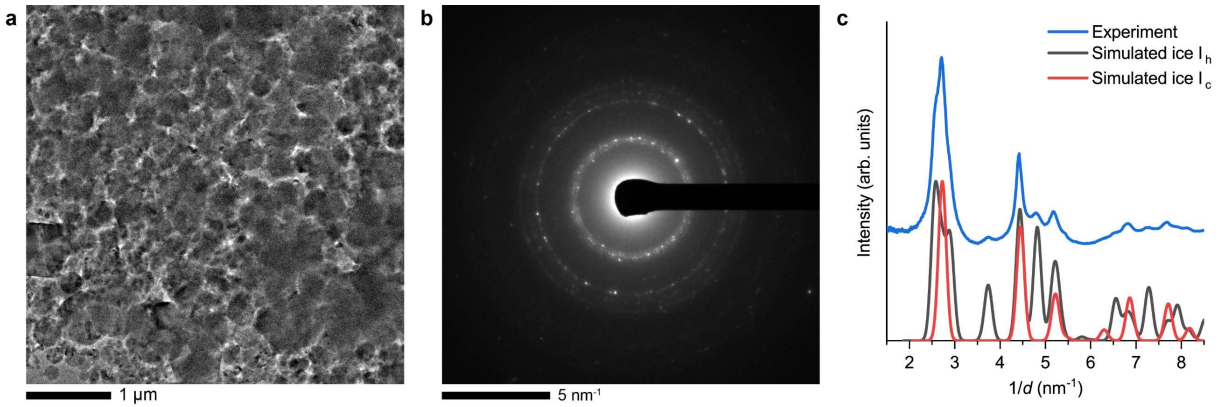
**Supplementary Fig. 2. XPS analysis of the carbon membrane.**

The water contact angle on the carbon membrane (supported on the Cu grid) was measured to be  $63.0^\circ \pm 1.8^\circ$  through drop-shape fitting<sup>2</sup> (Supplementary Fig. 3; independently measured on three grids). This result is similar to that on freshly exfoliated highly oriented pyrolytic graphite (HOPG) in air<sup>3</sup> and is consistent with the presence of mild oxidation and hydrocarbon adsorption on the membrane surface.

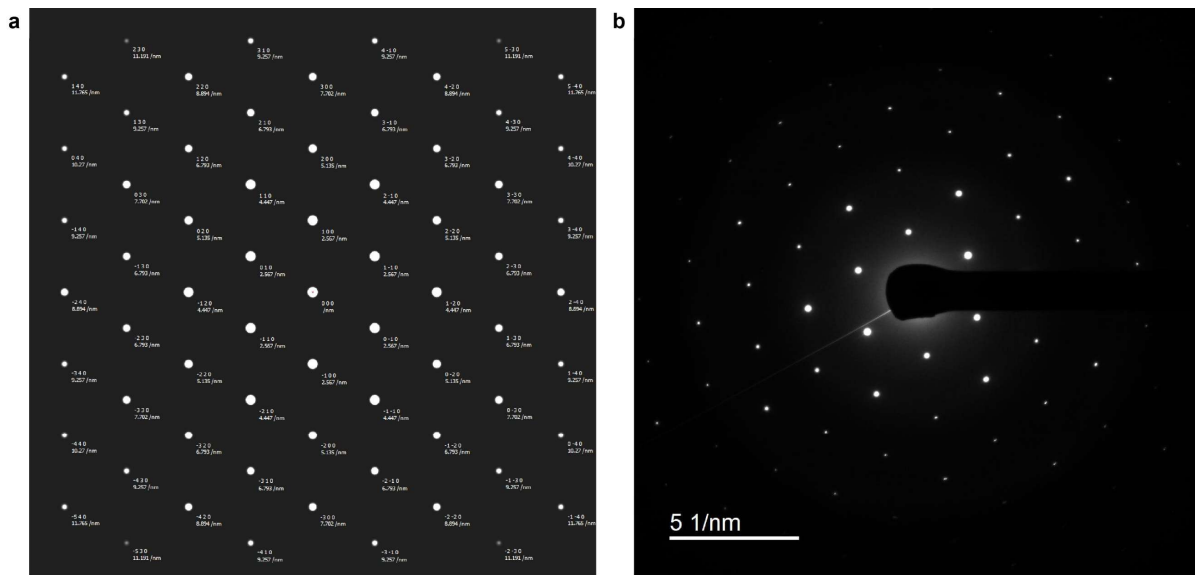


**Supplementary Fig. 3. Water contact angle measurement on carbon membrane.**

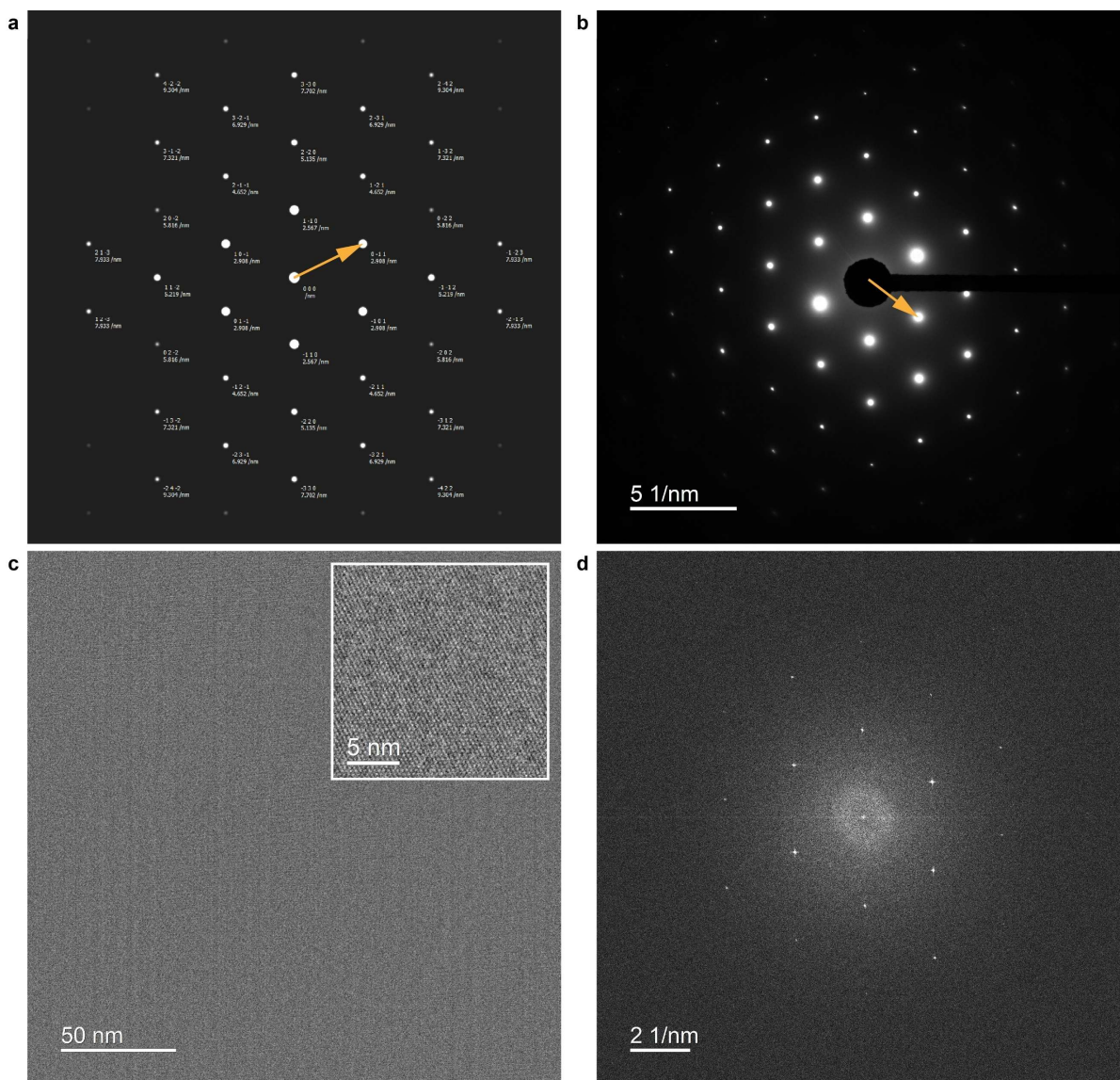
Sample crystallography



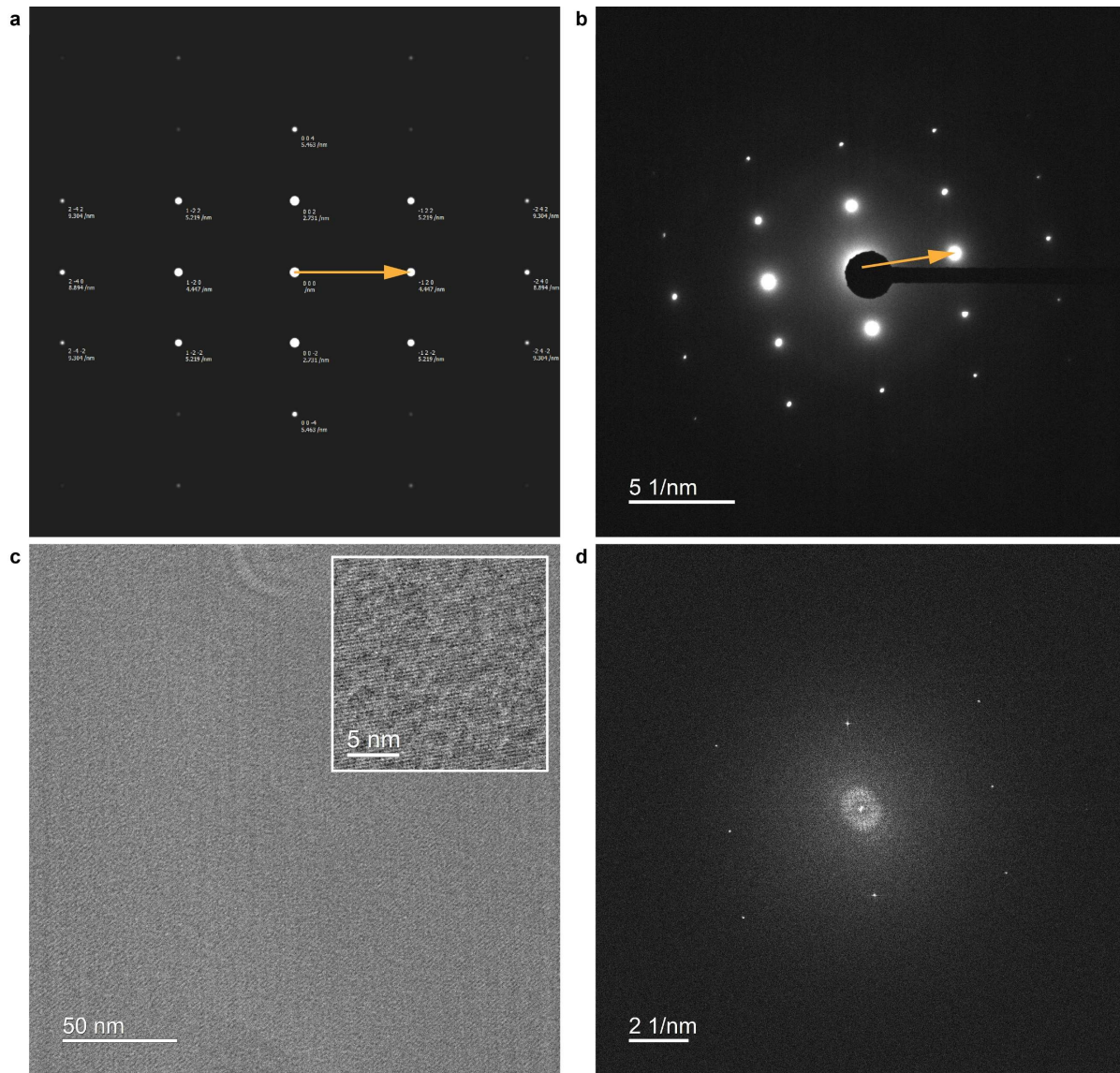
**Supplementary Fig. 4. Condensed ice crystallites made by exposing the cryogenic sample ( $< -180^\circ\text{C}$ ) in the air for a few seconds. a, TEM image. b, SAED pattern. c, Radial profile of the experimental SAED compared to the simulated patterns assuming ice  $I_h$  and  $I_c$ .**



**Supplementary Fig. 5. SAED of ice  $I_h$  along the  $[0001]$  zone axis. a, Dynamically simulated SAED. b, Experimental SAED.**



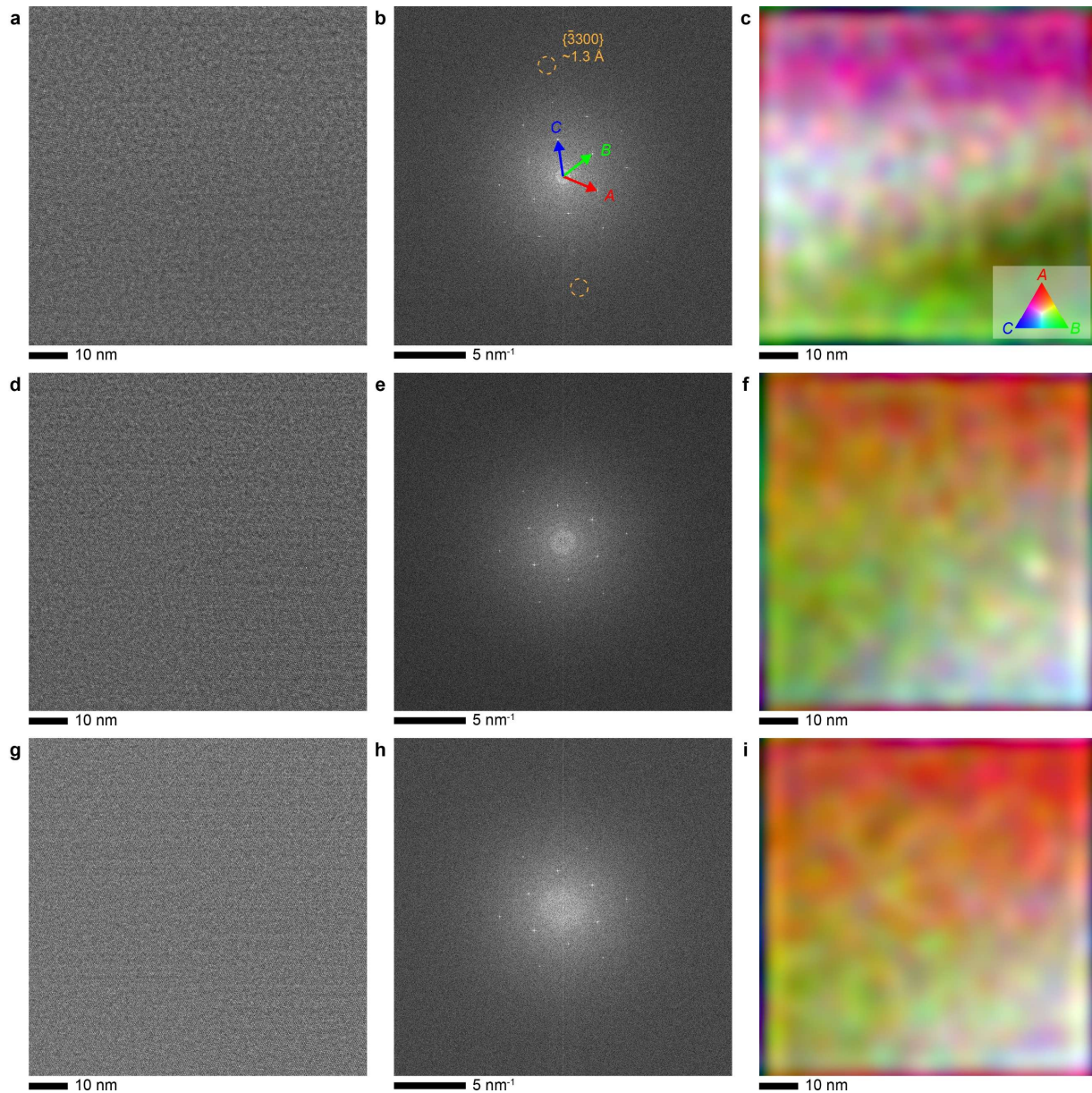
**Supplementary Fig. 6. SAED and HRTEM of ice  $I_h$  along the  $[11\bar{2}3]$  zone axis (Miller:  $[111]$ ).** **a**, Dynamically simulated SAED. **b**, Experimental SAED. **c**, ABS-filtered HRTEM image. Inset: enlarged image (see also Fig. 1e). **d**, Fourier transform of unfiltered HRTEM image. Arrows in **a** and **b** indicate the same reflections.



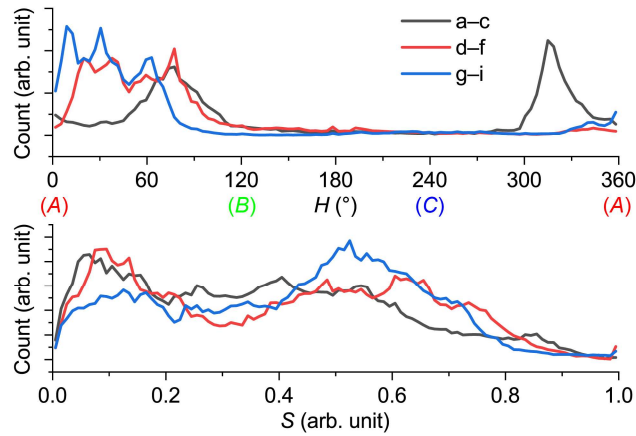
**Supplementary Fig. 7. SAED and HRTEM of ice  $I_h$  along the  $[10\bar{1}0]$  zone axis (Miller:  $[210]$ ).** **a**, Dynamically simulated SAED. **b**, Experimental SAED. **c**, ABS-filtered HRTEM image. Inset: enlarged image (see also Fig. 1f). **d**, Fourier transform of unfiltered HRTEM image. Arrows in **a** and **b** indicate the same reflections.



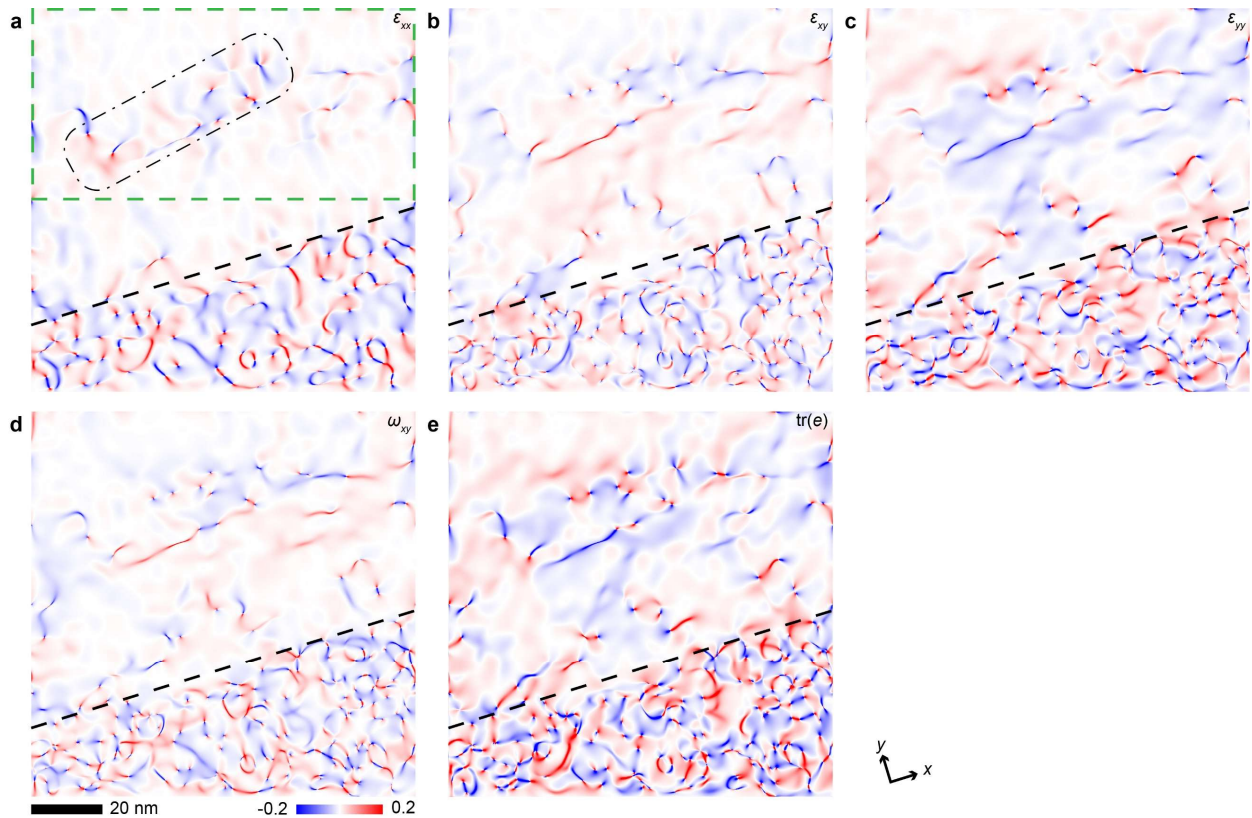
Lattice mapping



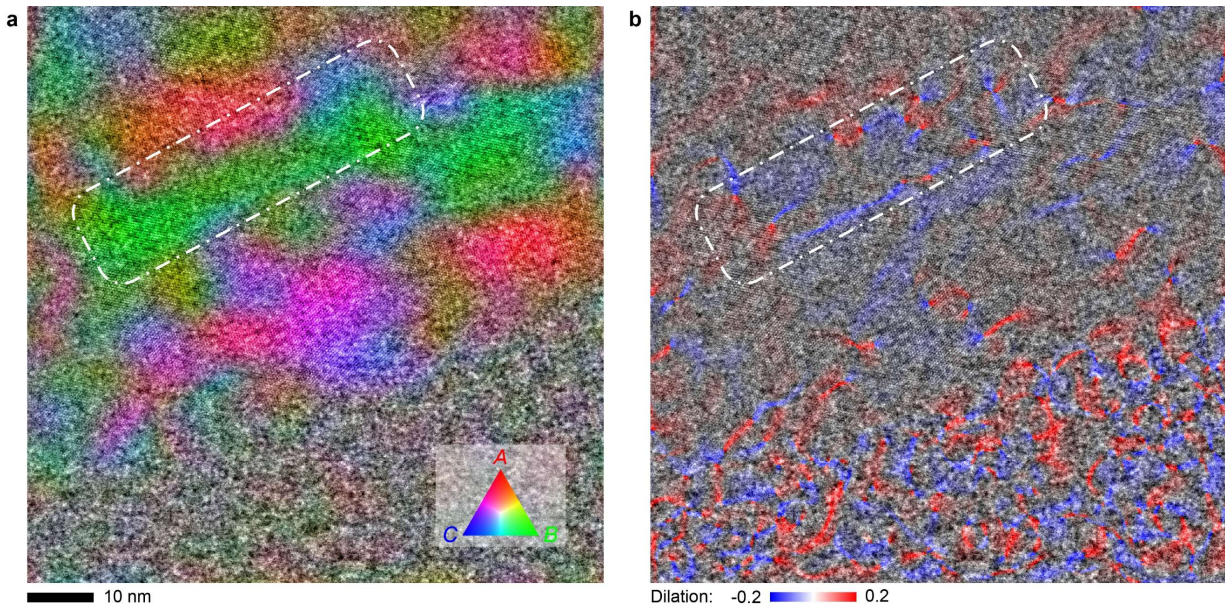
**Supplementary Fig. 8. High-resolution transmission electron microscopy (HRTEM) of a continuous hexagonal ice section along the [0001] zone axis with varying defocus (by row). a,d,g, ABS-filtered HRTEM images. b,e,h, Fourier transform of unfiltered HRTEM images. c,f,i, Lattice amplitude maps. All maps share the color coding specified in b and c. A negative defocus was applied and reduced toward zero from a to d and g. For case a, see also Fig. 1d.**



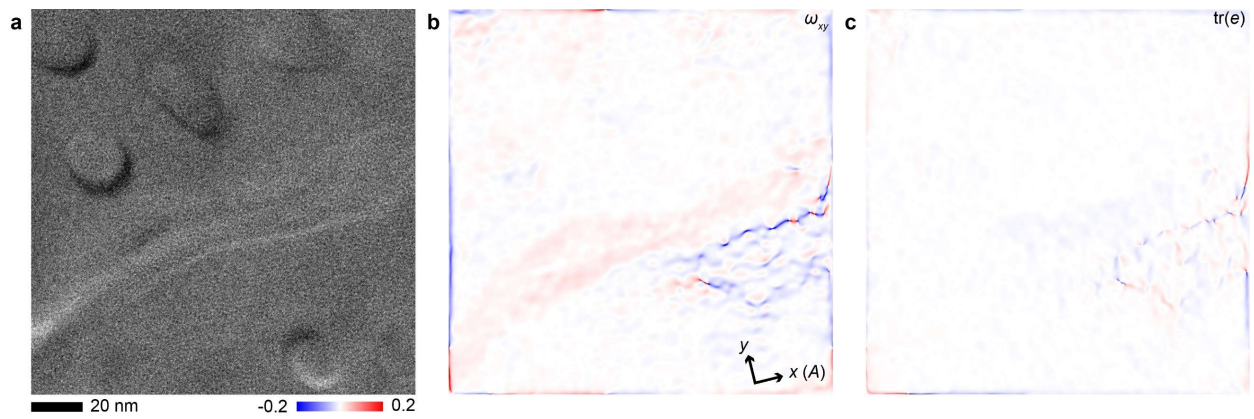
**Supplementary Fig. 9. Histograms of pixel hue (upper) and saturation (lower) in the hue-saturation-intensity (HSI) model of images in Supplementary Fig. 8.**



**Supplementary Fig. 10. In-plane geometric phase analysis for the defective edge. a, Strain  $\epsilon_{xx}$ . b, Strain  $\epsilon_{xy}$ . c, Strain  $\epsilon_{yy}$ . d, Rotation  $\omega_{xy}$ . e, Dilation  $\text{tr}(e)$ . A green dashed box in **a** indicates the area used to generate the histogram (Fig. 4h). Dot-dashes in **a** indicate a strip-shaped area with concentrated strains in the surroundings.**



**Supplementary Fig. 11. Color-painted ABS-filtered HRTEM images of the defective edge. a,** Lattice amplitude. **b,** Lattice dilation. Dot-dashes indicate the same area defined in Supplementary Fig. 10.



**Supplementary Fig. 12. Additional lattice maps for the ice section shown in Fig. 4. a,** HRTEM. **b,** Lattice rotation. **c,** Lattice dilation.

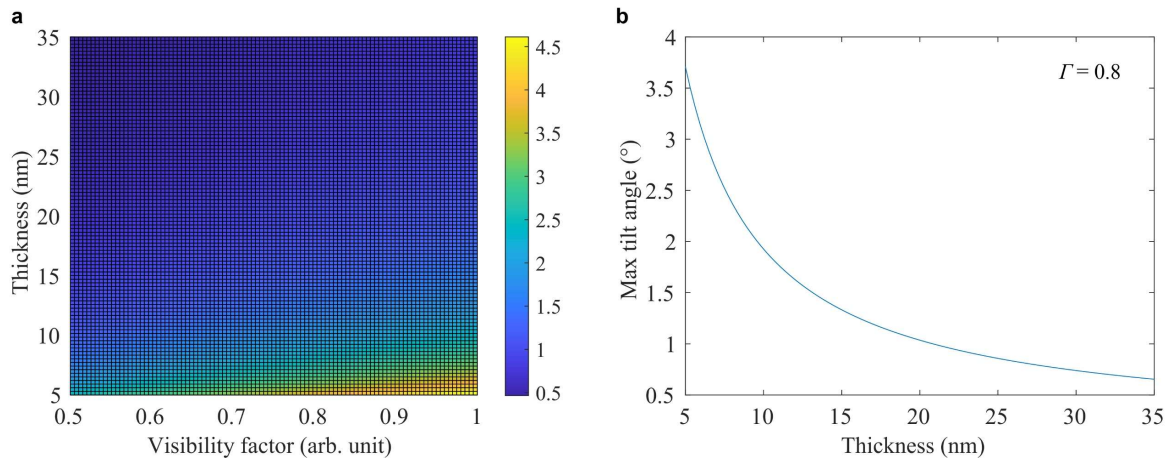
### Lattice fringe visibility band

A quick way to calculate the visibility of a certain lattice fringe from HRTEM images is to evaluate the intersection between the Ewald sphere and the diffraction spot in the reciprocal space. With kinematic approximation, the upper limit of the half angle to keep such an intersection is<sup>4</sup>:

$$\alpha_{\max} = \sin^{-1} \left\{ d \frac{\Gamma}{t} + \frac{\lambda}{2d} \left[ 1 - \left( d \frac{\Gamma}{t} \right)^2 \right] \right\}$$

### Supplementary Eq. 1

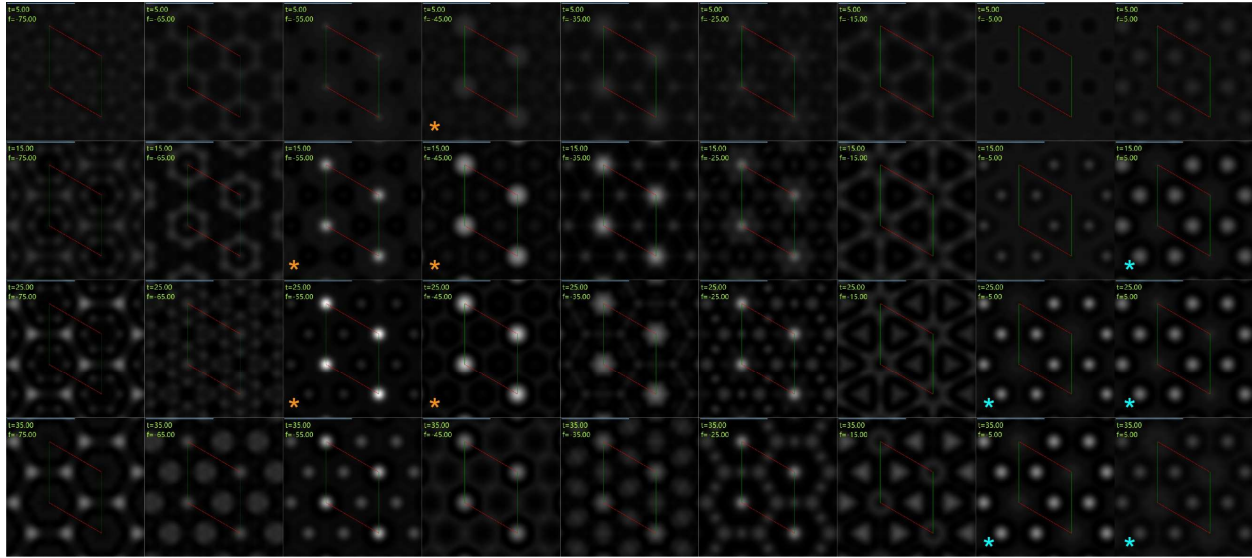
Here,  $d = 0.3895$  nm is the lattice spacing of ice  $\{\bar{1}100\}$ ,  $\Gamma$  is a visibility factor on the order of 1 relevant to the imaging and detection conditions,  $t$  is the crystal thickness,  $\lambda = 1.97$  pm is the electron beam wavelength at 300 kV. This calculation shows that to observe the ice  $\{\bar{1}100\}$  lattices in HRTEM, the maximum tilt angle of the crystals is about  $1^\circ$  to  $2^\circ$  when crystal thickness is 10 to 20 nm (Supplementary Fig. 13).



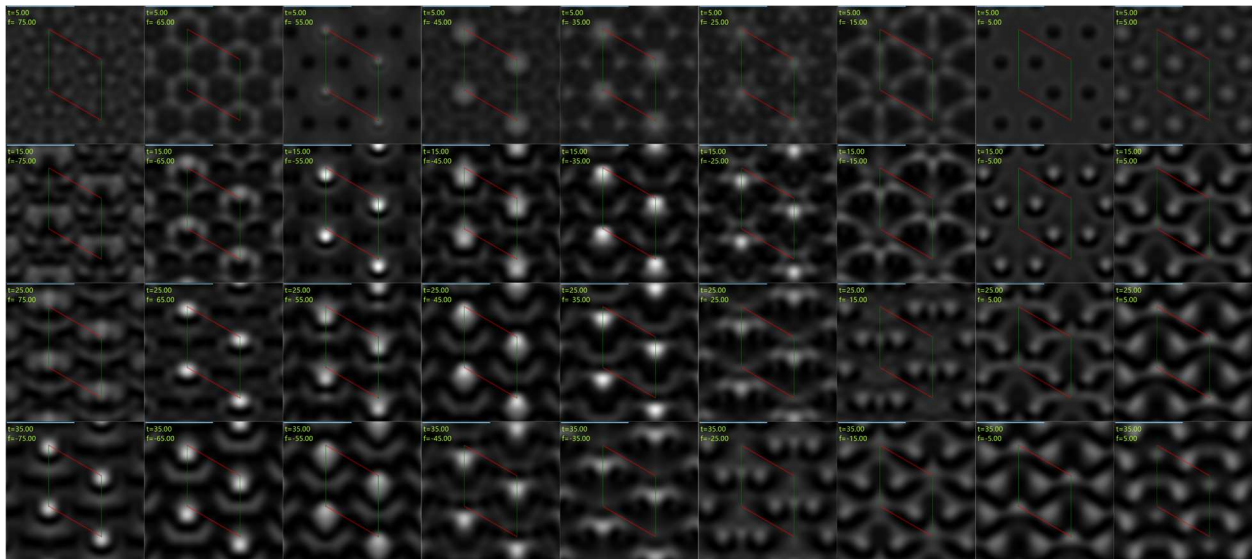
**Supplementary Fig. 13. Estimation of max tilt angle ( $^\circ$ ) for the visibility of ice  $\{\bar{1}100\}$  lattice fringes.**

**a**, Colormap as a function of the visibility factor ( $\Gamma$ ) and crystal thickness. **b**, Plot for visibility factor = 0.8.

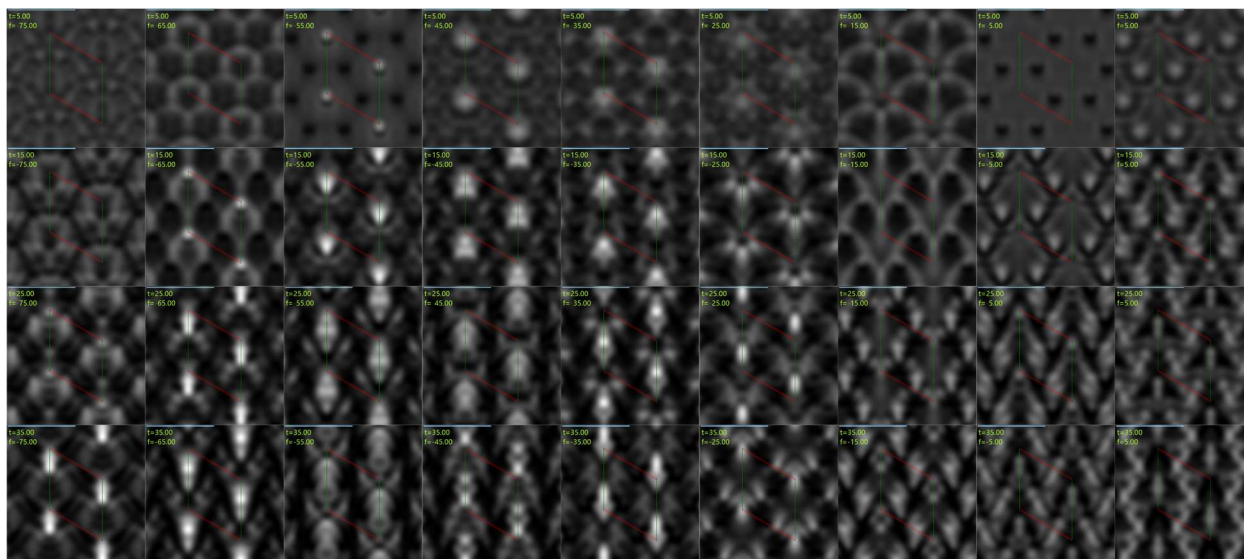
*Kinematical TEM simulation: low defocus*



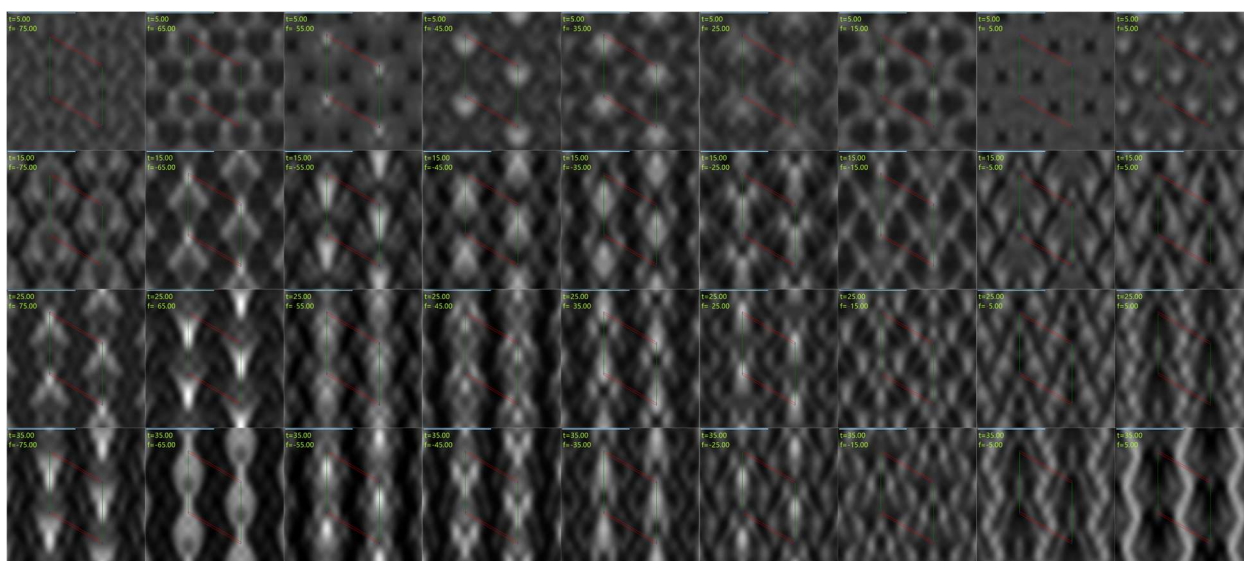
**Supplementary Fig. 14.** Kinematically simulated HRTEM image matrix of ice  $I_h$  along the  $[0001]$  zone axis. Thickness ( $t$ ) varies from 5 to 35 nm (by row). Defocus ( $f$ ) varies from  $-75$  to  $+5$  nm (by column). Scale bars (cyan): 0.5 nm. A unit cell is outlined in each image. Orange and cyan asterisks note two types of patterns commonly observed in the experiments.



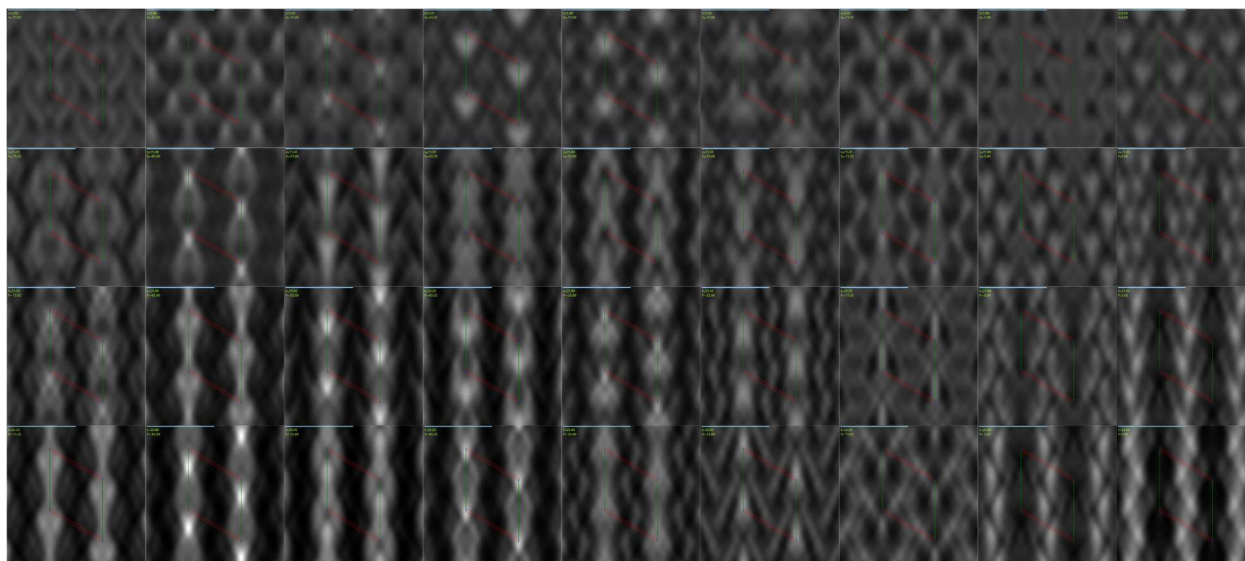
**Supplementary Fig. 15.** Kinematically simulated HRTEM image matrix of ice  $I_h$  along the  $[0001]$  zone axis tilted by  $0.4^\circ$  towards the  $a_2$ -axis direction (vertical). Thickness ( $t$ ) varies from 5 to 35 nm (by row). Defocus ( $f$ ) varies from  $-75$  to  $+5$  nm (by column). Scale bars (cyan): 0.5 nm. A unit cell is outlined in each image.



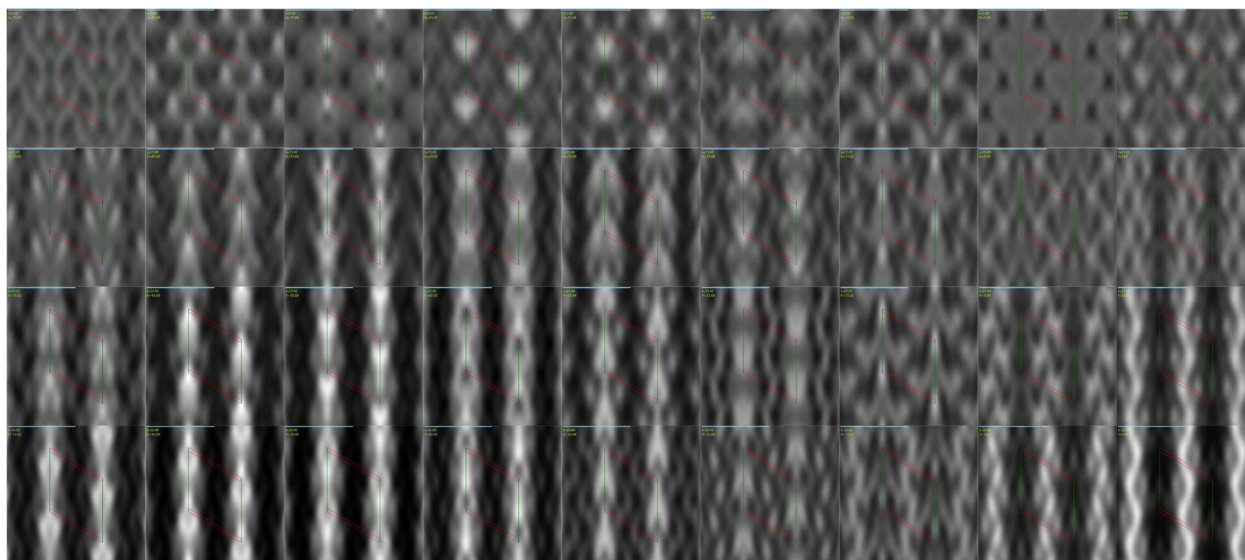
**Supplementary Fig. 16.** Kinematically simulated HRTEM image matrix of ice  $I_h$  along the  $[0001]$  zone axis tilted by  $0.8^\circ$  towards the  $a_2$ -axis direction (vertical). Thickness ( $t$ ) varies from 5 to 35 nm (by row). Defocus ( $f$ ) varies from  $-75$  to  $+5$  nm (by column). Scale bars (cyan): 0.5 nm. A unit cell is outlined in each image.



**Supplementary Fig. 17.** Kinematically simulated HRTEM image matrix of ice  $I_h$  along the  $[0001]$  zone axis tilted by  $1.2^\circ$  towards the  $a_2$ -axis direction (vertical). Thickness ( $t$ ) varies from 5 to 35 nm (by row). Defocus ( $f$ ) varies from  $-75$  to  $+5$  nm (by column). Scale bars (cyan): 0.5 nm. A unit cell is outlined in each image.



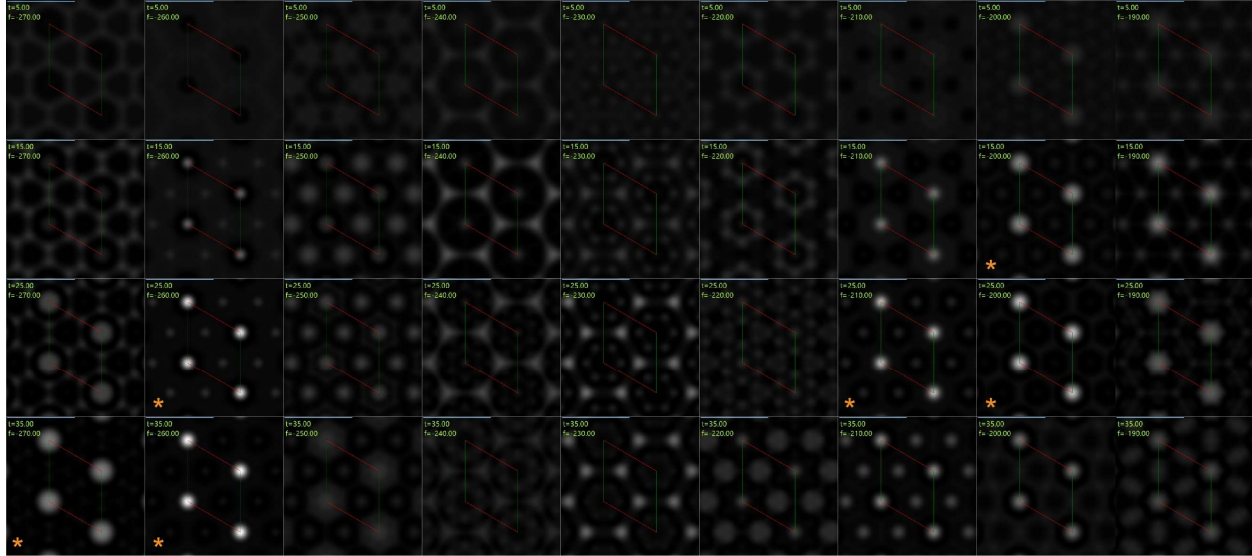
**Supplementary Fig. 18.** Kinematically simulated HRTEM image matrix of ice  $I_h$  along the  $[0001]$  zone axis tilted by  $1.6^\circ$  towards the  $a_2$ -axis direction (vertical). Thickness ( $t$ ) varies from 5 to 35 nm (by row). Defocus ( $f$ ) varies from  $-75$  to  $+5$  nm (by column). Scale bars (cyan): 0.5 nm. A unit cell is outlined in each image.



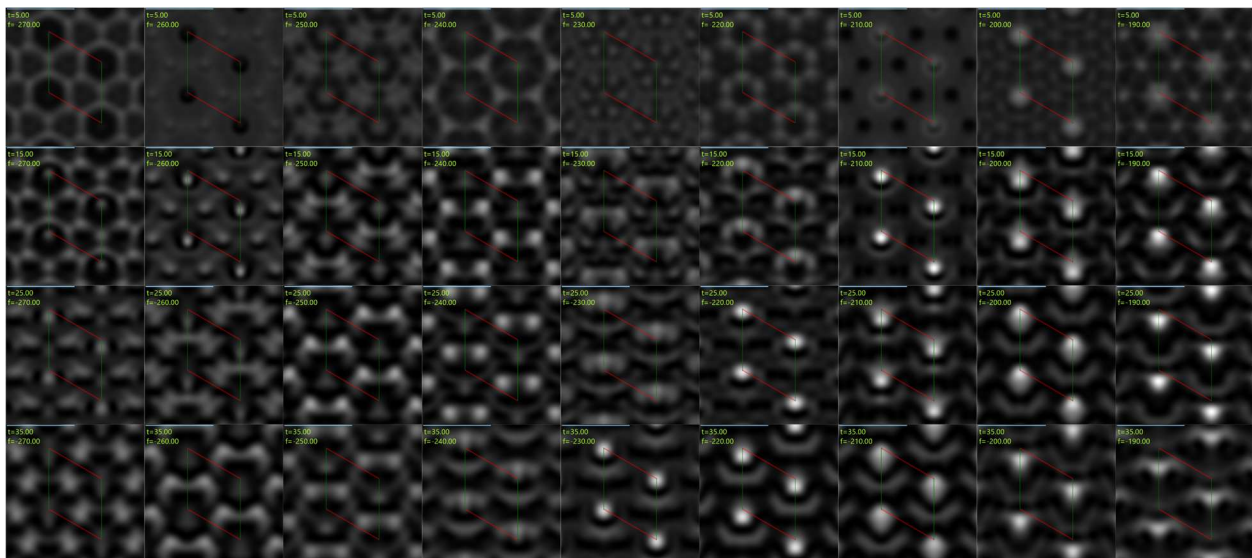
**Supplementary Fig. 19.** Kinematically simulated HRTEM image matrix of ice  $I_h$  along the  $[0001]$  zone axis tilted by  $2.0^\circ$  towards the  $a_2$ -axis direction (vertical). Thickness ( $t$ ) varies from 5 to 35 nm (by row). Defocus ( $f$ ) varies from  $-75$  to  $+5$  nm (by column). Scale bars (cyan): 0.5 nm. A unit cell is outlined in each image.

*Kinematical TEM simulation: high defocus*

While imaging the highly defective, thin crystal edges (Fig. 2), a slightly larger defocus than what is typically used for materials samples is applied to provide sufficient image contrast from ice. In this specific case, fitting the contrast transfer function of the HRTEM image<sup>5</sup> results in defocus values of  $-271$  and  $-240$  nm. Therefore, we further performed kinematical TEM simulations under high-defocus conditions as below.

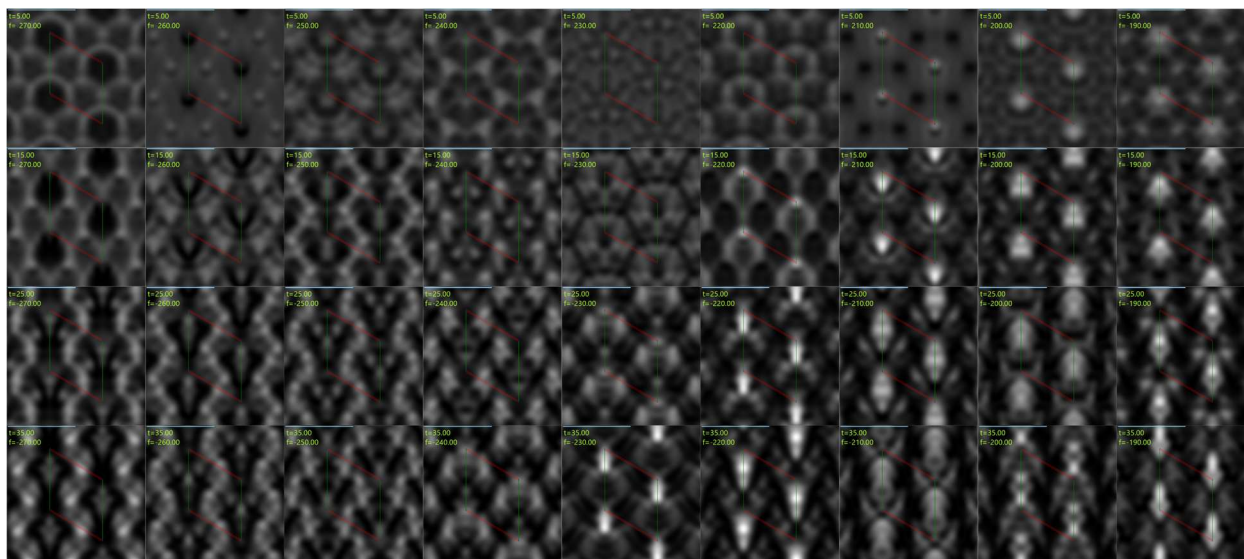


**Supplementary Fig. 20.** Kinematically simulated HRTEM image matrix with high defocus of ice  $I_h$  along the  $[0001]$  zone axis. Thickness ( $t$ ) varies from 5 to 35 nm (by row). Defocus ( $f$ ) varies from  $-270$  to  $-190$  nm (by column). Scale bars (cyan): 0.5 nm. A unit cell is outlined in each image. Orange asterisks note patterns matching experimental observations.

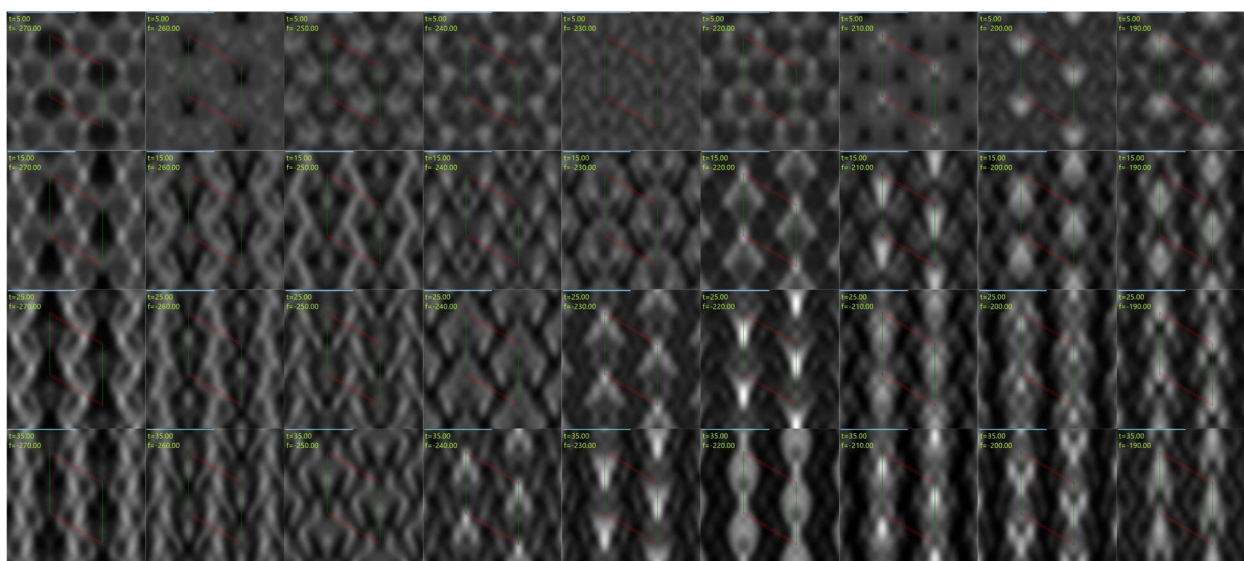


**Supplementary Fig. 21.** Kinematically simulated HRTEM image matrix with high defocus of ice  $I_h$  along the  $[0001]$  zone axis tilted by  $0.4^\circ$  towards the  $a_2$ -axis direction (vertical). Thickness ( $t$ ) varies from 5 to 35 nm (by row). Defocus ( $f$ ) varies from  $-270$  to  $-190$  nm (by column). Scale bars (cyan): 0.5 nm. A unit cell is outlined in each image.

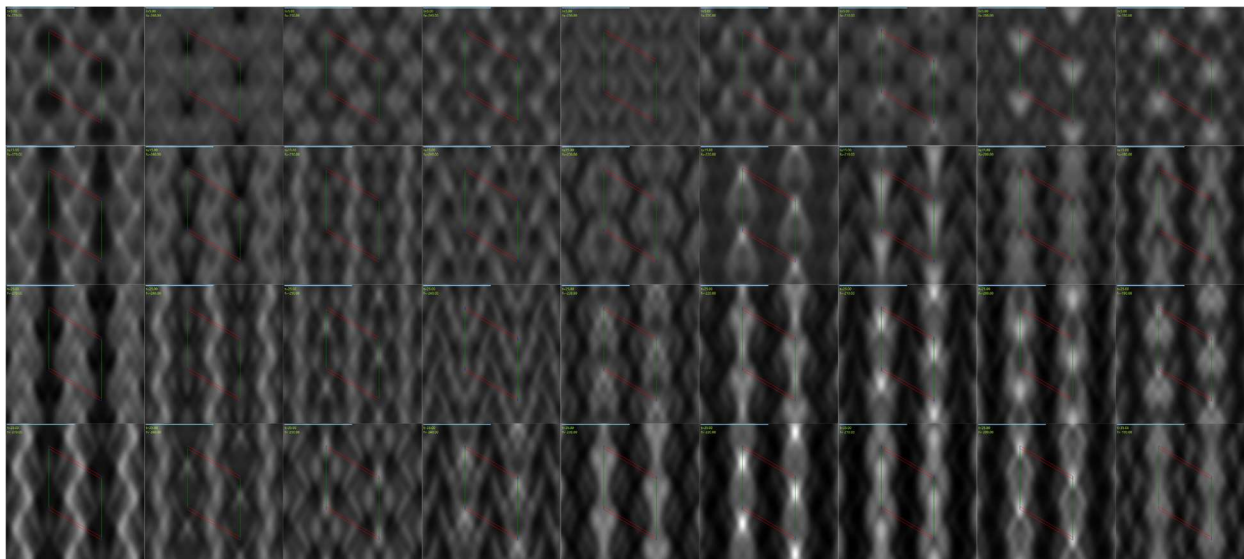




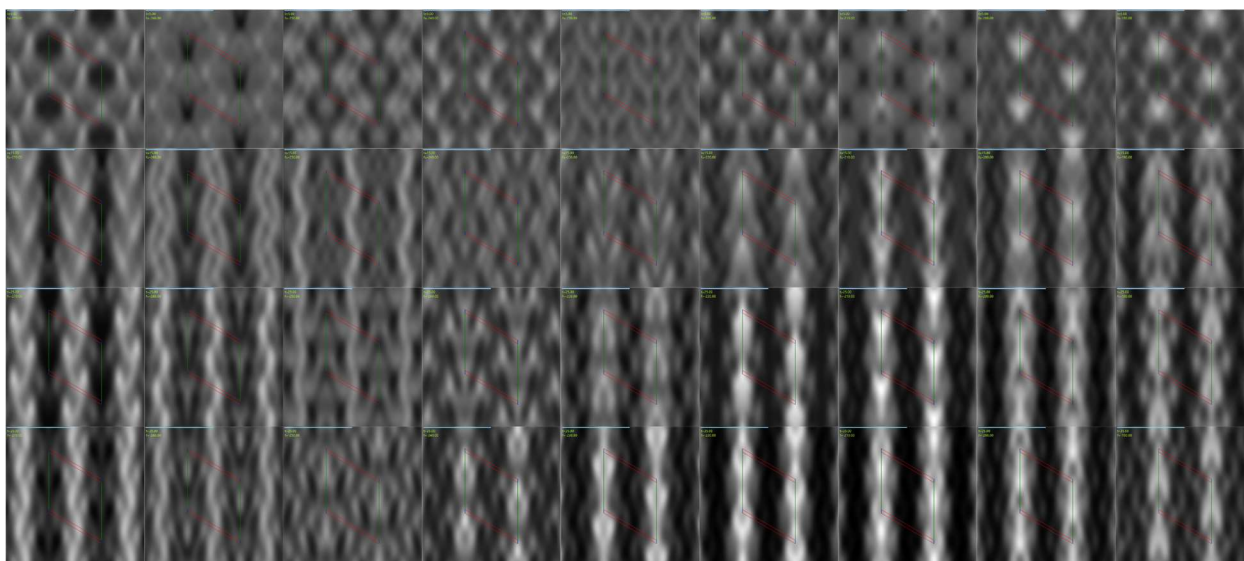
**Supplementary Fig. 22.** Kinetically simulated HRTEM image matrix with high defocus of ice  $I_h$  along the  $[0001]$  zone axis tilted by  $0.8^\circ$  towards the  $a_2$ -axis direction (vertical). Thickness ( $t$ ) varies from 5 to 35 nm (by row). Defocus ( $f$ ) varies from  $-270$  to  $-190$  nm (by column). Scale bars (cyan): 0.5 nm. A unit cell is outlined in each image.



**Supplementary Fig. 23.** Kinetically simulated HRTEM image matrix with high defocus of ice  $I_h$  along the  $[0001]$  zone axis tilted by  $1.2^\circ$  towards the  $a_2$ -axis direction (vertical). Thickness ( $t$ ) varies from 5 to 35 nm (by row). Defocus ( $f$ ) varies from  $-270$  to  $-190$  nm (by column). Scale bars (cyan): 0.5 nm. A unit cell is outlined in each image.

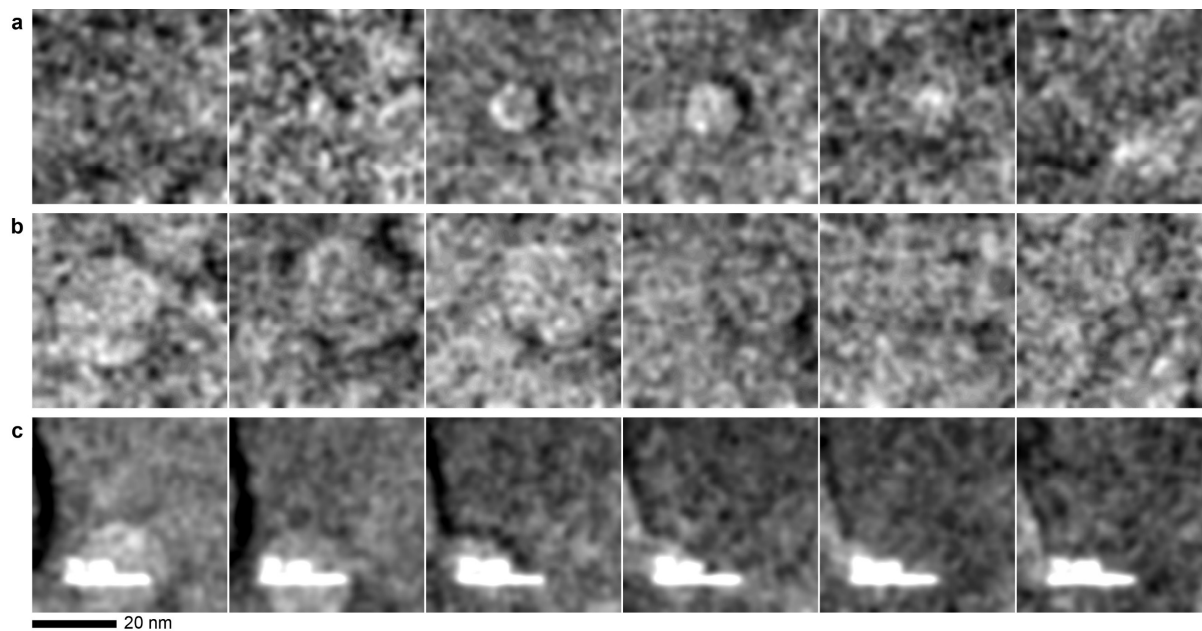


**Supplementary Fig. 24. Kinematically simulated HRTEM image matrix with high defocus of ice  $I_h$  along the  $[0001]$  zone axis tilted by  $1.6^\circ$  towards the  $a_2$ -axis direction (vertical). Thickness ( $t$ ) varies from 5 to 35 nm (by row). Defocus ( $f$ ) varies from  $-270$  to  $-190$  nm (by column). Scale bars (cyan): 0.5 nm. A unit cell is outlined in each image.**



**Supplementary Fig. 25. Kinematically simulated HRTEM image matrix with high defocus of ice  $I_h$  along the  $[0001]$  zone axis tilted by  $2.0^\circ$  towards the  $a_2$ -axis direction (vertical). Thickness ( $t$ ) varies from 5 to 35 nm (by row). Defocus ( $f$ ) varies from  $-270$  to  $-190$  nm (by column). Scale bars (cyan): 0.5 nm. A unit cell is outlined in each image.**

*Bubble dynamics*

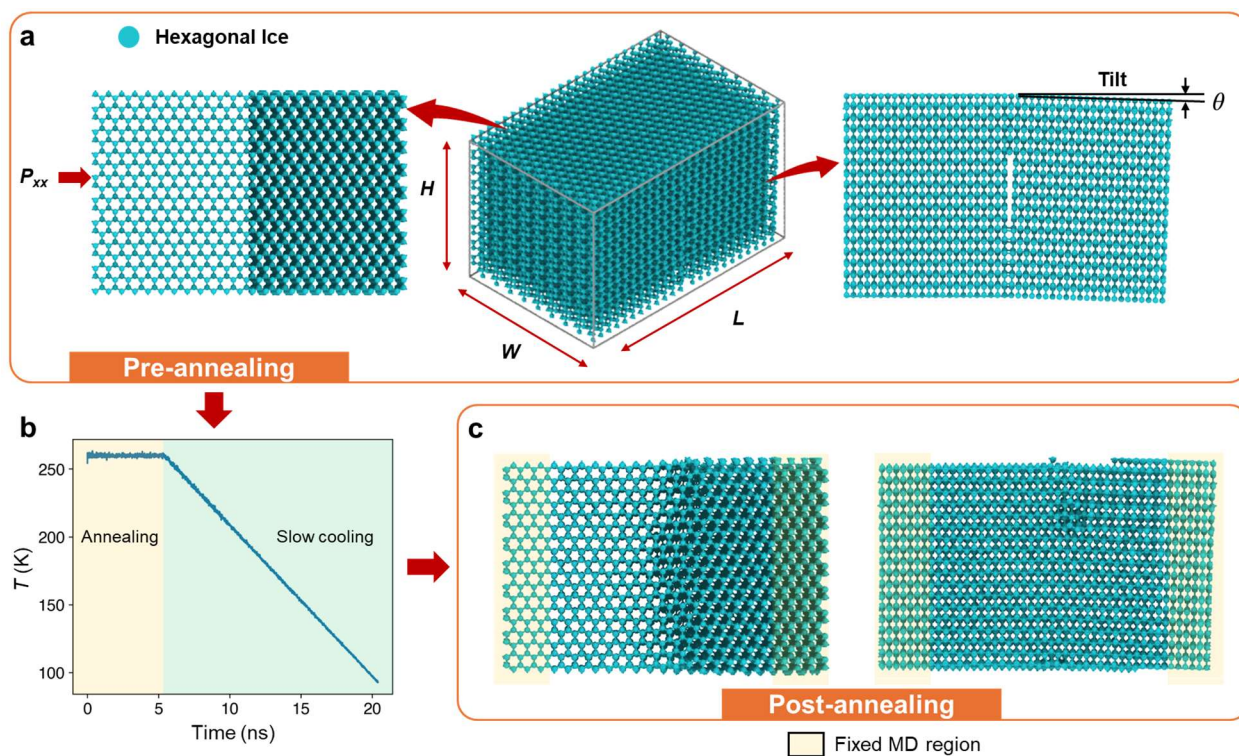


**Supplementary Fig. 26. Lowpass-filtered HRTEM images for Fig. 5a to c.** Cutoff frequency:  $0.05 \text{ pixel}^{-1}$  ( $0.465 \text{ nm}^{-1}$ ). White features in **c** are due to the embedded scale bars in the screen recording.

## Supplementary Details for Molecular Dynamics Simulation

### *MD simulation details for tilt boundaries*

To better understand the relationship between the tilt angle of the boundaries and their thermodynamic stability, we conducted MD simulations at temperatures emulating the experimental conditions. As depicted in Supplementary Fig. 27a, the simulation setup begins with a block of hexagonal ice with dimensions ( $L, H, W$ ). We note that we have simulation setups for four different sizes with dimensions (105, 69, 21), (105, 69, 43), (105, 69, 65), (105, 69, 130), and finally a larger size (132, 69, 261). All dimensions are in Å. It is to be noted that for all the cases, the dimensions primarily vary along the height of the box. We denote these in terms of replication of the original unit cell of the hexagonal ice we started with as  $(4 \times 3 \times 1)$ ,  $(4 \times 3 \times 2)$ ,  $(4 \times 3 \times 3)$ ,  $(4 \times 3 \times 6)$ ,  $(5 \times 3 \times 12)$ . We tilted the half section of the initial block with the desired tilt angle. Depending on the size of the supercell, different concentrations of defects for the same tilt angle were introduced. We then used an annealing protocol to relax these boundaries and bring them to the desired temperatures, as depicted in Supplementary Fig. 27b. A typical annealed boundary is shown in Supplementary Fig. 27c. Different replication sizes are used to have a different degree of defect concentration in the starting configuration. As there is an inherent mismatch between tilted surfaces, this introduces defects.



**Supplementary Fig. 27. The overall MD simulation setup for grain boundaries.** **a**, In the pre-annealing stage, a tilt angle boundary of the hexagonal ice is created by rotating the half section of the hexagonal ice block around the  $a_2$  axis. **b**, Typical annealing profile used during the simulation. **c**, Top (left) and front (right) view of the final annealed configuration of a typical model.

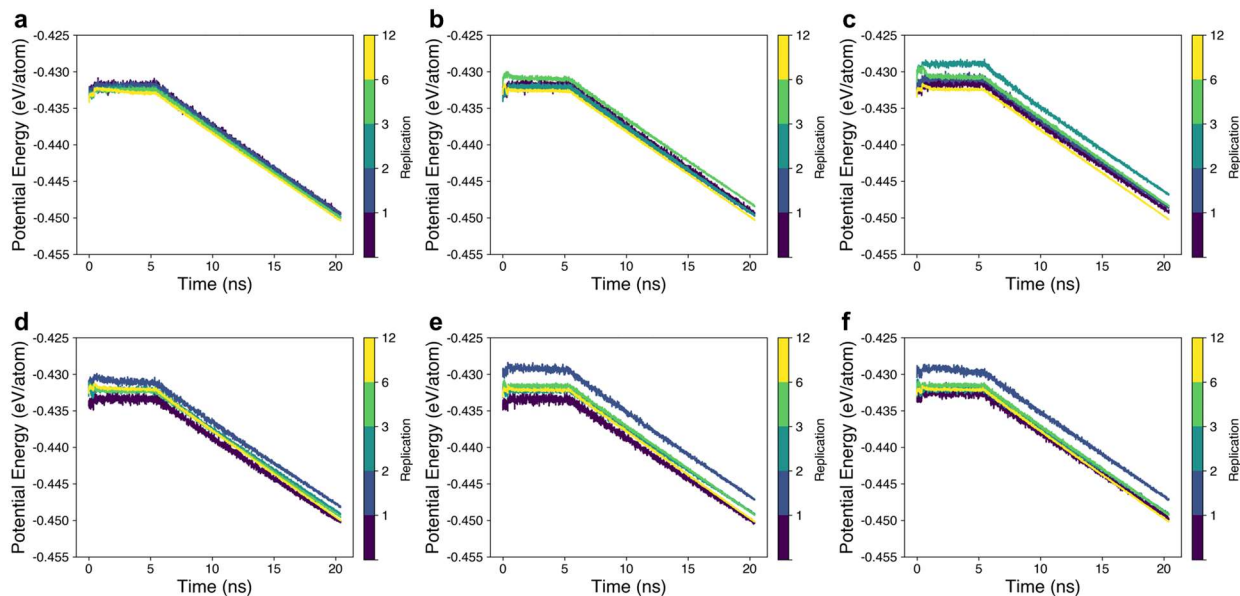
Water molecules are represented as coarse-grained beads, where each molecule is simplified to one bead placed at the oxygen atom position with hydrogen atoms removed. Interactions between these water beads are described by a machine-learned Tersoff bond-order potential<sup>6</sup>, which captures the properties of water phases with reasonable agreement with experiments. For a starting supercell configuration, we minimized it locally with the conjugate gradient algorithm<sup>7</sup> on the ML-BOP potential energy surface. The LAMMPS package<sup>8</sup> is used for all molecular dynamic simulations in the  $NVE$  ensemble. It is important to note that the particles at both ends of the simulation box were fixed during the time integration by setting their resultant forces to zero (Supplementary Fig. 27c). This was done to retain the initial tilt angle, mimicking two large grains with the desired tilt. Our focus is on the boundary region where two grains meet. Therefore, a Langevin thermostat was applied between the fixed sections. Additionally, we maintained a fixed pressure of 0 atm along  $P_{xx}$  (Supplementary Fig. 27a). The setup's post-minimized configuration was first annealed at 260 K to allow faster system relaxation and diffusion of defects at the boundary. This temperature was held for 5 ns, and then the system was gradually cooled to 93 K in the next 15 ns (Supplementary Fig. 27b). Finally, the pre- and post-annealing angles and energetics were computed.

To calculate the tilt angle between the minimized and post-annealing configurations, we began by selecting two spherical sections near the center from each side (tilted and non-tilted) of the simulation box for the initial, minimized, and relaxed configurations. These sections are essentially sets of Cartesian coordinates represented by  $(N \times 3)$  matrices. To determine the optimal rotation and translation between two sets of corresponding 3D point data, we sought the best transformation that aligns the points in matrix  $A$  to matrix  $B$ . This transformation is often referred to as the Euclidean or Rigid transform because it preserves shape and size. To find the angle, we need to determine the rotation matrix  $R$ . As we have only rotation in one direction, we can calculate the tilt from the rotation matrix afterward. Singular value decomposition (SVD) can be used to find the subsequent rotation matrix<sup>9</sup>. We obtained a covariance matrix  $H$  such that:

$$\begin{aligned}
 H &= (A - \text{Centroid}_A)(B - \text{Centroid}_B)^T \\
 [U, S, V] &= \text{SVD}(H) \\
 R &= VU^T
 \end{aligned}$$

### Supplementary Eq. 2

Supplementary Fig. 28 shows the variation of potential energy for different sizes and tilt angles throughout the simulation duration. It can be observed that during the annealing time of the first 5 ns, the potential energy remains constant and decreases subsequently as the system cools down. One noticeable aspect is that at lower tilt angles (Supplementary Fig. 28a and b), the energies of all sizes almost overlap. This is because the concentration of defects at lower tilt angles, irrespective of the size of the supercell, is very low. As the tilt angle increases, so does the dislocation defect concentration with the increase in the supercell size (Supplementary Fig. 28c to f). This causes varying energies for different sizes as the simulation progresses. We note that for almost all cases, the largest supercell ( $5 \times 4 \times 12$ ) eventually reaches an energy lower than all of its peers. This reveals that low-angle boundaries can be stabilized by dislocations with very low energy penalties. Rather than increasing the boundary energy, higher tilt angles lead to the creation of new dislocations, resulting in a reduction of the system's energy. This allows for the formation of diverse interfaces without incurring significant penalties.



**Supplementary Fig. 28. Variation of the potential energy with time for different sizes of configurations and tilt angles.** Plotted are the potential energy per molecule against the simulation time for initial tilt angles of  $0.2^\circ$  (a),  $0.6^\circ$  (b),  $1.2^\circ$  (c),  $1.6^\circ$  (d),  $1.8^\circ$  (e), and  $2.0^\circ$  (f), respectively.

**Supplementary Table 1. Equilibrated tilt angle and mean cohesive energy of the low-angle grain boundary with  $t = 1$  from the MD simulation at 93 K after annealing.**

| Initial Tilt ( $^\circ$ ) | Equilibrated Tilt ( $^\circ$ ) | Mean Cohesive Energy (eV/atom) |
|---------------------------|--------------------------------|--------------------------------|
| 0.0                       | 0.66305                        | -0.45054                       |
| 0.2                       | 0.48696                        | -0.44938                       |
| 0.4                       | 0.12359                        | -0.44939                       |
| 0.6                       | 0.31435                        | -0.44940                       |
| 0.8                       | 0.03098                        | -0.44919                       |
| 1.0                       | 0.06518                        | -0.44929                       |
| 1.2                       | 0.34492                        | -0.44917                       |
| 1.4                       | 0.13814                        | -0.44833                       |
| 1.6                       | 0.07485                        | -0.45018                       |
| 1.8                       | 0.22442                        | -0.45034                       |
| 2.0                       | 0.58875                        | -0.44976                       |

**Supplementary Table 2. Equilibrated tilt angle and mean cohesive energy of the low-angle grain boundary with  $t = 2$  from the MD simulation at 93 K after annealing.**

| Initial Tilt ( $^\circ$ ) | Equilibrated Tilt ( $^\circ$ ) | Mean Cohesive Energy (eV/atom) |
|---------------------------|--------------------------------|--------------------------------|
| 0.0                       | 0.1754                         | -0.45058                       |
| 0.2                       | 0.11199                        | -0.44949                       |
| 0.4                       | 0.01689                        | -0.44979                       |
| 0.6                       | 0.39062                        | -0.44970                       |
| 0.8                       | 0.18748                        | -0.44959                       |

|     |         |          |
|-----|---------|----------|
| 1.0 | 0.50077 | -0.44990 |
| 1.2 | 0.4724  | -0.44861 |
| 1.4 | 0.26985 | -0.44863 |
| 1.6 | 0.3494  | -0.44812 |
| 1.8 | 0.36574 | -0.44715 |
| 2.0 | 3.11576 | -0.44710 |

**Supplementary Table 3. Equilibrated tilt angle and mean cohesive energy of the low-angle grain boundary with  $t = 3$  from the MD simulation at 93 K after annealing.**

| Initial Tilt (°) | Equilibrated Tilt (°) | Mean Cohesive Energy (eV/atom) |
|------------------|-----------------------|--------------------------------|
| 0.0              | 0.13170               | -0.45052                       |
| 0.2              | 0.13512               | -0.44989                       |
| 0.4              | 0.17156               | -0.44985                       |
| 0.6              | 0.32064               | -0.44963                       |
| 0.8              | 0.46252               | -0.44925                       |
| 1.0              | 0.69297               | -0.44750                       |
| 1.2              | 0.83801               | -0.44683                       |
| 1.4              | 2.10579               | -0.44770                       |
| 1.6              | 1.98957               | -0.44914                       |
| 1.8              | 1.91082               | -0.44920                       |
| 2.0              | 2.10446               | -0.44913                       |

**Supplementary Table 4. Equilibrated tilt angle and mean cohesive energy of the low-angle grain boundary with  $t = 4$  from the MD simulation at 93 K after annealing.**

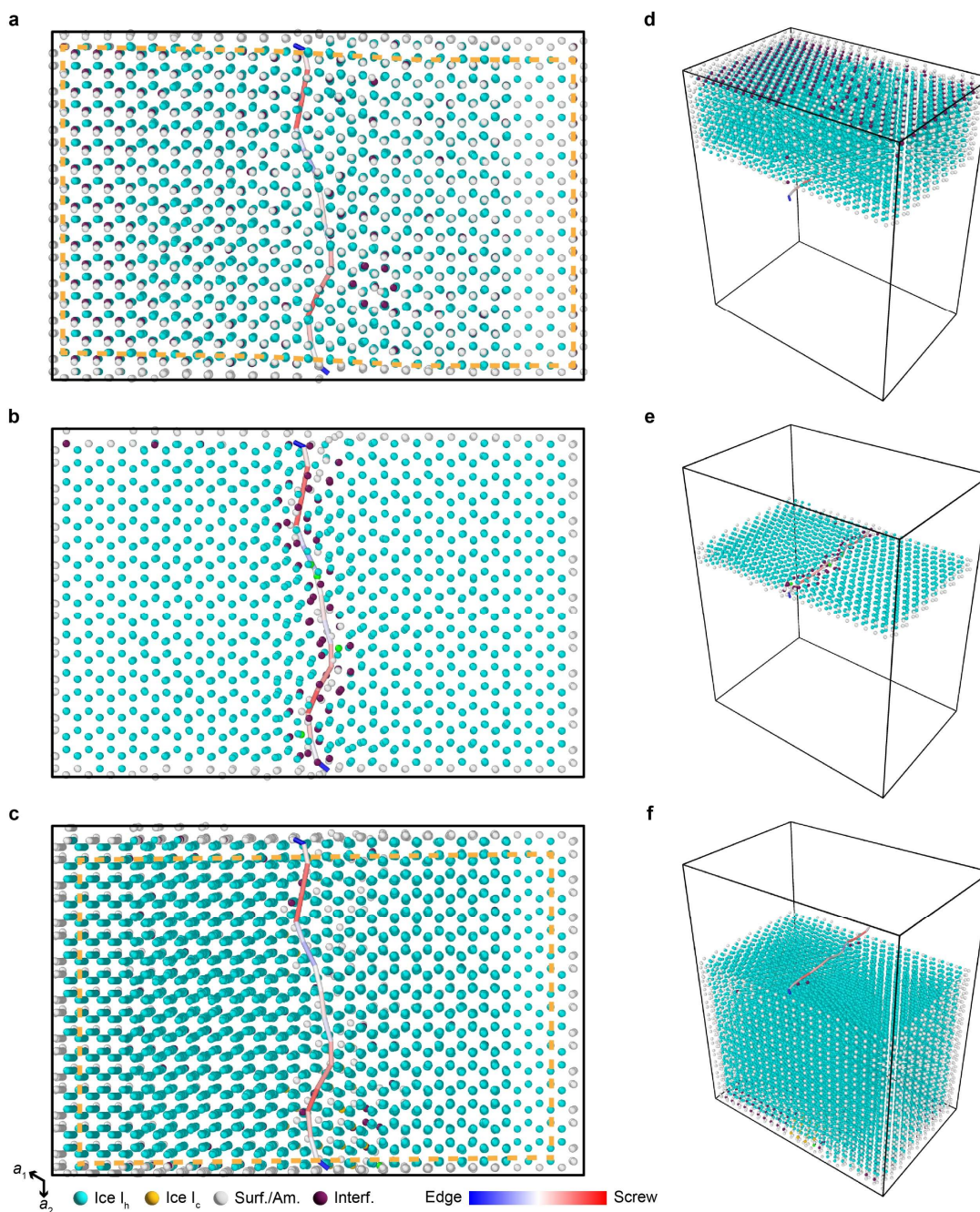
| Initial Tilt (°) | Equilibrated Tilt (°) | Mean Cohesive Energy (eV/atom) |
|------------------|-----------------------|--------------------------------|
| 0.0              | 0.02520               | -0.45052                       |
| 0.2              | 0.09408               | -0.45003                       |
| 0.4              | 0.33899               | -0.44908                       |
| 0.6              | 0.81075               | -0.44841                       |
| 0.8              | 0.85889               | -0.44882                       |
| 1.0              | 0.96212               | -0.44890                       |
| 1.2              | 1.47930               | -0.44839                       |
| 1.4              | 1.87475               | -0.44880                       |
| 1.6              | 1.69638               | -0.44951                       |
| 1.8              | 1.93293               | -0.44924                       |
| 2.0              | 2.28449               | -0.44921                       |

**Supplementary Table 5. Equilibrated tilt angle and mean cohesive energy of the low-angle grain boundary with  $t = 5$  from the MD simulation at 93 K after annealing.**

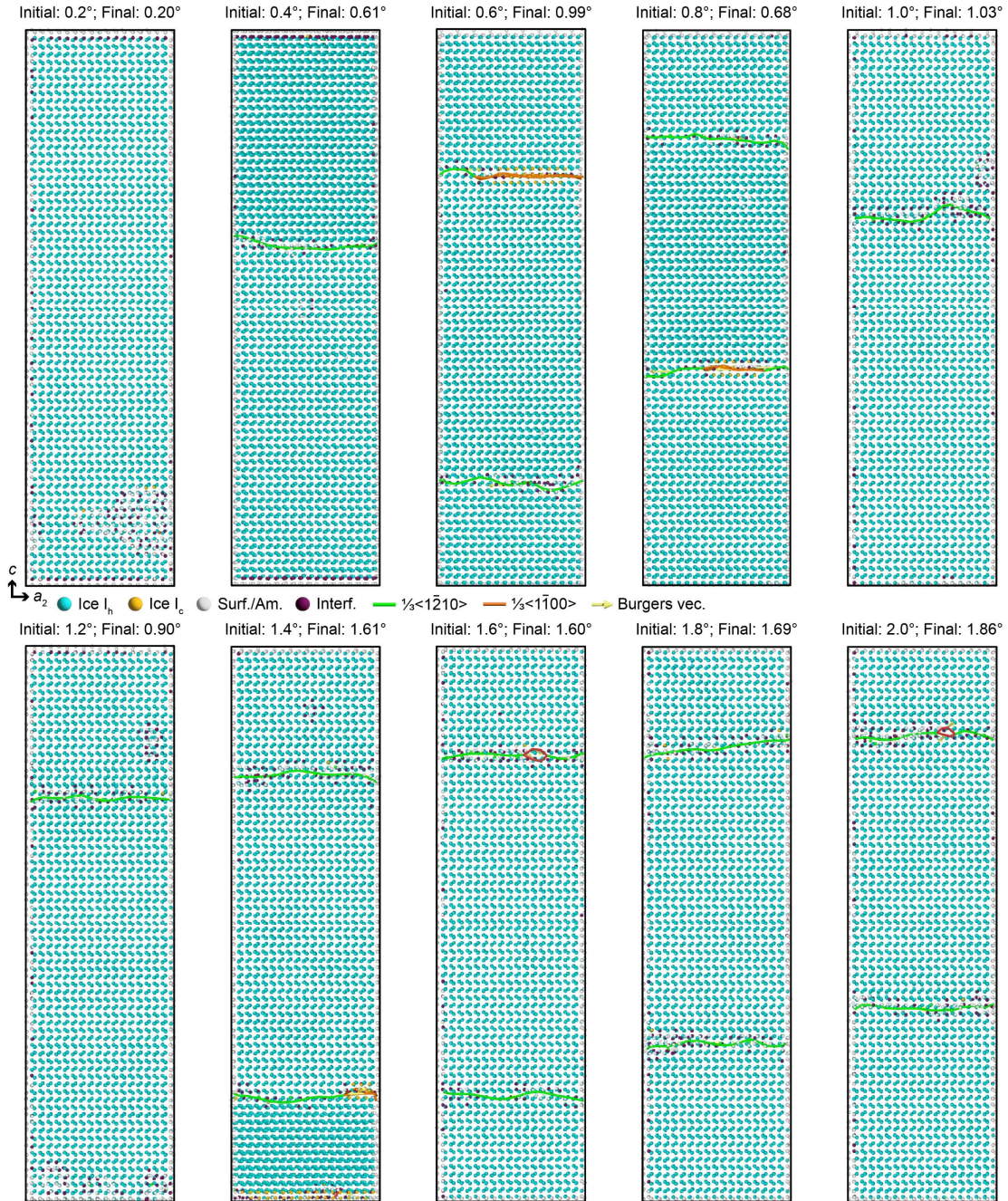
| Initial Tilt (°) | Equilibrated Tilt (°) | Mean Cohesive Energy (eV/atom) |
|------------------|-----------------------|--------------------------------|
| 0.0              | 0.01754               | -0.45151                       |
| 0.2              | 0.19995               | -0.45041                       |

|     |         |          |
|-----|---------|----------|
| 0.4 | 0.61409 | -0.45023 |
| 0.6 | 0.99410 | -0.45027 |
| 0.8 | 0.68264 | -0.45034 |
| 1.0 | 1.03049 | -0.45048 |
| 1.2 | 0.89977 | -0.45023 |
| 1.4 | 1.61049 | -0.45021 |
| 1.6 | 1.60362 | -0.45000 |
| 1.8 | 1.68874 | -0.45018 |
| 2.0 | 1.85593 | -0.45017 |





**Supplementary Fig. 29. Structural analysis of the mixed screw and edge dislocation from the MD simulation ( $t = 6$ , initial tilt angle =  $1.0^\circ$ , final tilt angle =  $0.96^\circ$ ).** **a–c**, Top view of the cross-sectional models of the upper domain (**a**), interfacial layers (**b**), and the lower domain (**c**). Orange dashes outline the lattices and show the half-plane mismatch between the upper and the lower domains. **d–f**, Corresponding perspective models. Beads: water molecules in ice, surface/amorphous (surf./am.), interfacial (interf.), or hydrate-like local configurations (other colors). The local character of the dislocation is quantified by a color scale (blue-white-red).



**Supplementary Fig. 30. Cross-sectional models of the tilted ice ( $t = 12$ ) with various tilt angles.** Beads: water molecules in ice, surface/amorphous (surf./am.), interfacial (interf.), or hydrate-like local configurations (other colors). Red lines represent dislocations of other types.

### MD simulation details for bubbles/cavities

We conducted molecular dynamics (MD) simulation of nanobubbles using LAMMPS in a 20 nm × 20 nm × 20 nm orthogonal simulation box with periodic boundary conditions. To create the initial structure of a nanobubble, we start with a hexagonal ice crystal lattice with its (1 $\bar{1}$ 00), (11 $\bar{2}$ 0), and (0001) planes, i.e., 1<sup>st</sup> prism, 2<sup>nd</sup> prism, and basal planes, normal to the x-, y-, and z-axes of the simulation box. Water molecules within a 6 nm distance from the center of the simulation box are removed to form the nanobubble.

Subsequently, the initial nanobubble structure undergoes energy minimization and equilibration for 50 ps in an isothermal-isobaric ensemble at a temperature of 260 K and pressure of 1 bar. In this equilibration step and all subsequent steps, the simulation timestep is set to 5 fs, and the Nose-Hoover thermostat and barostat damping time constants are set to 0.1 ps and 1.0 ps, respectively. After the initial equilibration, a series of fixed-volume (canonical ensemble) equilibrations are applied only to the water beads within a 9 nm distance from the center of the simulation box. This process involves heating for 0.5 ns to raise the temperature from 260 K to 270 K, followed by a 50 ps structural relaxation at 370 K, a 10 ns quenching step to decrease the temperature from 370 K back to 260 K, and finally, a 2 ns structural relaxation at 260 K to obtain the final structure of the static nanobubble.

### Facet recognition for bubbles

Water molecules in the first crystalline layer on the surface of the simulated static nanobubble are labeled as one of three hexagonal ice surface types (basal, primary prism, and secondary prism) based on a score for each water molecule. This score deduces if its neighbors within a 6-Å cutoff radius lie on a plane parallel to any of the ice surface planes. To determine the scores, we first obtain unit normal vectors of the families of Miller-Bravais planes  $\{hkil\}$  relevant to the hexagonal ice surfaces. Since the x-, y-, and z-axes of our simulation box are normal to the (1 $\bar{1}$ 00), (11 $\bar{2}$ 0), and (0001) planes of the simulated hexagonal ice crystal lattice, the unique unit vectors,  $\hat{n}$ , for non-parallel planes are [0, 0, 1] for the (0001) basal planes, [1/2,  $\sqrt{3}/2$ , 0], [1, 0, 0], [1/2,  $-\sqrt{3}/2$ , 0] for the (10 $\bar{1}$ 0), (1 $\bar{1}$ 00), (0 $\bar{1}$ 10) 1<sup>st</sup> prism planes, and [0, 1, 0], [ $\sqrt{3}/2$ , 1/2, 0], [ $\sqrt{3}/2$ , -1/2, 0] for the (11 $\bar{2}$ 0), (2 $\bar{1}$ 10), (1 $\bar{2}$ 10) 2<sup>nd</sup> prism planes. For every water molecule, we compute all vectors between point **A** (the molecule itself) and point **B** (its neighbors) and calculate the cosine between these vectors and the surface normal vector through the dot product,

$$\text{cosine}_{hkil} = \overline{\mathbf{AB}}_{\text{unit}} \cdot \hat{n}.$$

### **Supplementary Eq. 3**

For a given molecule, if it were to lie on a given plane, the unit vector  $\overline{\mathbf{AB}}_{\text{unit}}$  for all the neighboring molecules should be perpendicular to the surface normal vector, making the cosine close to 0.

Additionally, to account for thermal noise, a lower standard deviation among their cosine distances means that they will be parallel to the surface, and this facet is more prominent. Thus, the final score is determined as follows:

$$\text{score}_{hkil} = \text{SD}(\text{cosine}_{hkil}^p \in p = 1, \dots, N) + \text{mean}(\text{cosine}_{hkil}^p \in p = 1, \dots, N).$$

### **Supplementary Eq. 4**

We repeat the same process for all surface normal vectors and assign the surface type labels based on two criteria. If the overall score is > 0.6, do not assign the molecule to any surface; otherwise, assign the molecule to the surface having the lowest score associated with it.

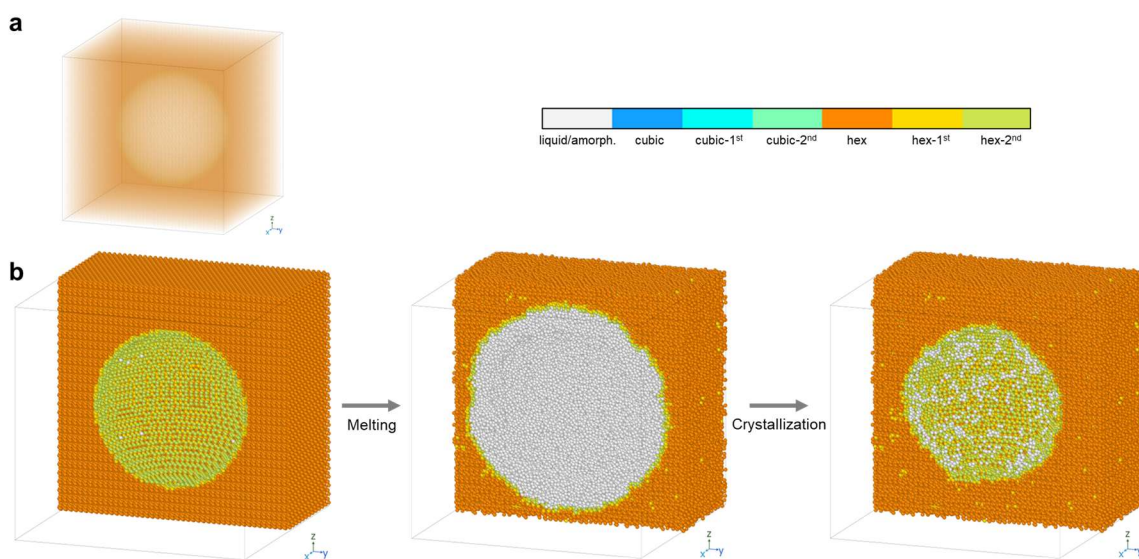
### Surface energy calculation

The individual slabs with the  $c$  lattice vector oriented normal to the target plane were constructed using Python libraries pymatgen<sup>10</sup> and spglib<sup>11</sup> from a unit cell of hexagonal ice ( $I_h$ ). The energies of the unit cell and the slab were computed using the LAMMPS, employing the ML-BOP model<sup>6</sup>. The surface energy for a facet with Miller-Bravais indices  $\{hkl\}$  is:

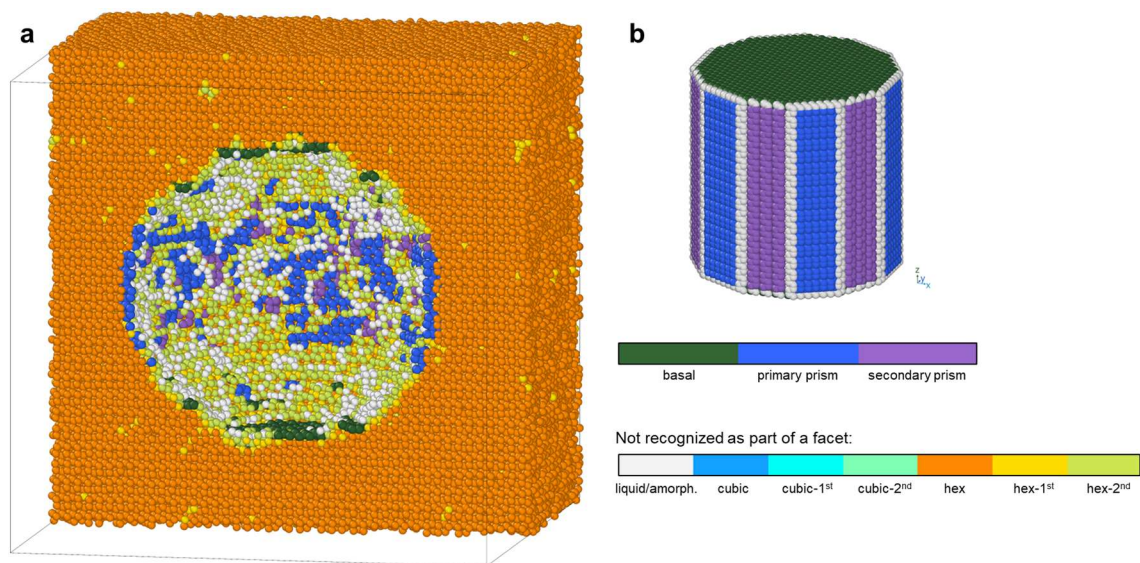
$$SE_{hkl} = \frac{E_{\text{slab}} - nE_{\text{pa,unit}}}{2A},$$

### Supplementary Eq. 5

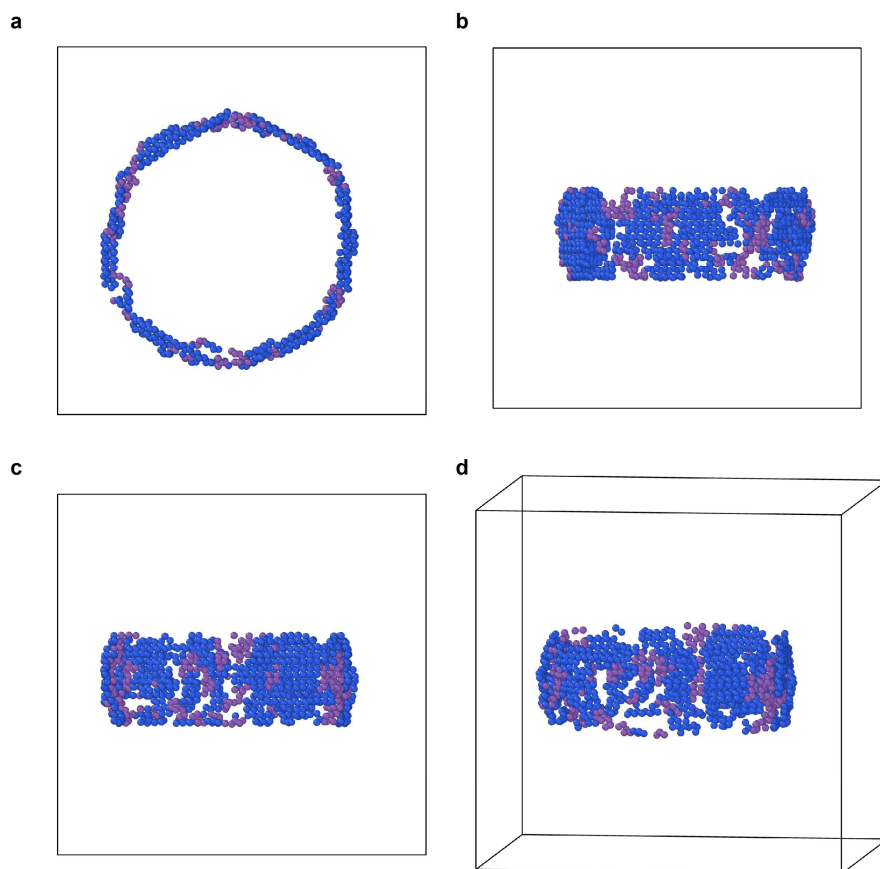
where  $E_{\text{slab}}$  is the total cohesive energy of the slab,  $n$  is the number of molecules in the slab,  $E_{\text{pa,unit}}$  is the energy per molecule of the unit cell of hexagonal ice, and  $A$  is the exposed surface area of the slab.



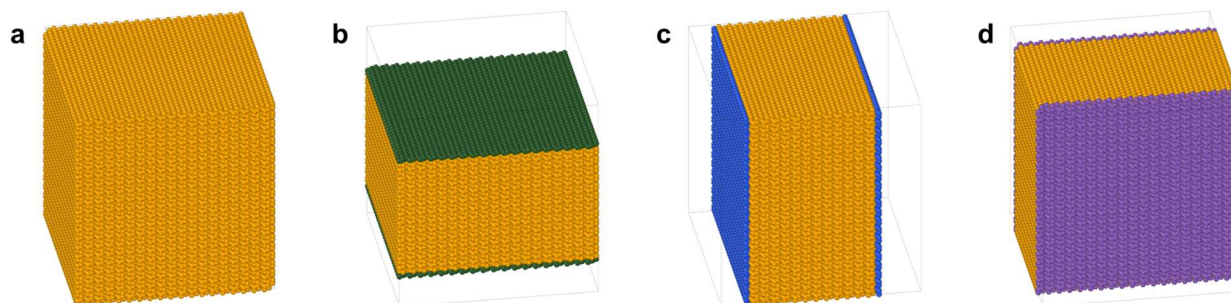
**Supplementary Fig. 31. MD modeling of a nanobubble in ice  $I_h$ .** **a**, Illustration of the initial setup with a spherical cavity inside an ice crystal. **b**, Cross-sectional view of the model in the MD simulation for obtaining an equilibrated structure. Color coding represents the local environment of the molecules. Labels “-1<sup>st</sup>” and “-2<sup>nd</sup>” refer to molecules that are the first or second nearest neighbors of another molecule that has been identified as a cubic or hexagonal lattice site, but at least one of the nearest neighbors is not at a lattice site.



**Supplementary Fig. 32. Facet recognition of MD-simulated nanobubble. a, Cross-sectional model. b, Color-coding for facets illustrated in a prismatic crystal.**



**Supplementary Fig. 33. Cross-section (5-nm in the center) of MD-simulated bubble surface colored by recognized facets in different views. a, Top. b, Left. c, Front. d, 3D. Vertical direction: *c*-axis.**



**Supplementary Fig. 34. MD models used for evaluating surface energies of different facets. a,** Bulk crystal. **b,** Basal planes. **c,** Primary prism planes. **d,** Secondary prism planes.

**Supplementary Table 6. Summary of surface energy calculations from MD. PE: cohesive energy.**

| Surface type    | # of molecules | PE (eV)    | Surface area ( $\text{\AA}^2$ ) | PE <sub>surface</sub> (meV/ $\text{\AA}^2$ ) |
|-----------------|----------------|------------|---------------------------------|--|
| Bulk reference  | 105335         | -48826.249 | 0                               | 0  |
| Basal           | 67715          | -31107.526 | 43340.01                        | 6.475  |
| Primary prism   | 72071          | -33100.841 | 45162.60                        | 6.785  |
| Secondary prism | 71819          | -32938.276 | 45037.91                        | 7.820  |

## Supplementary Details for Theoretical Calculations

### Elastic strain

According to the continuum theories of elasticity<sup>12</sup>, for a spherical cavity (radius =  $R$ ) inside an isotropic material with an internal pressure of the cavity  $p_1$  and external pressure  $p_2$ , components of the strain tensor in spherical polar coordinates take the form of:

$$\varepsilon_{rr} = a - \frac{2b}{r^3}, \varepsilon_{\theta\theta} = \varepsilon_{\phi\phi} = a + \frac{b}{r^3}.$$

**Supplementary Eq. 6**

Accordingly, the radial stress is:

$$\sigma_{rr} = \frac{E}{1-2\nu}a - \frac{2E}{1+\nu}\frac{b}{r^3},$$

**Supplementary Eq. 7**

where  $E$  is the Young's modulus and  $\nu$  is the Poisson's ratio. Given stress boundary conditions  $\sigma_{rr}|_{r=R} = -p_1$  and  $\sigma_{rr}|_{r \rightarrow +\infty} = -p_2$ ,  $a$  and  $b$  are determined by:

$$a = \frac{p_2}{E}(2\nu - 1), b = \frac{p_1 - p_2}{2E}(1 + \nu)R^2.$$

**Supplementary Eq. 8**

Now we consider a Laplacian pressure caused by the spherical cavity surface:

$$\Delta P = p_1 - p_2 = \frac{2\gamma}{R},$$

**Supplementary Eq. 9**

and assume atmospheric pressure outside the material  $p_2 = p^\emptyset$ . Plugging these values into Supplementary Eq. 6 gives:

$$\begin{aligned} \varepsilon_{rr} &= \frac{p^\emptyset}{E}(2\nu - 1) + \frac{2\gamma R^2}{Er^3}(1 + \nu), \\ \varepsilon_{\theta\theta} = \varepsilon_{\phi\phi} &= \frac{p^\emptyset}{E}(2\nu - 1) - \frac{\gamma R^2}{Er^3}(1 + \nu). \end{aligned}$$

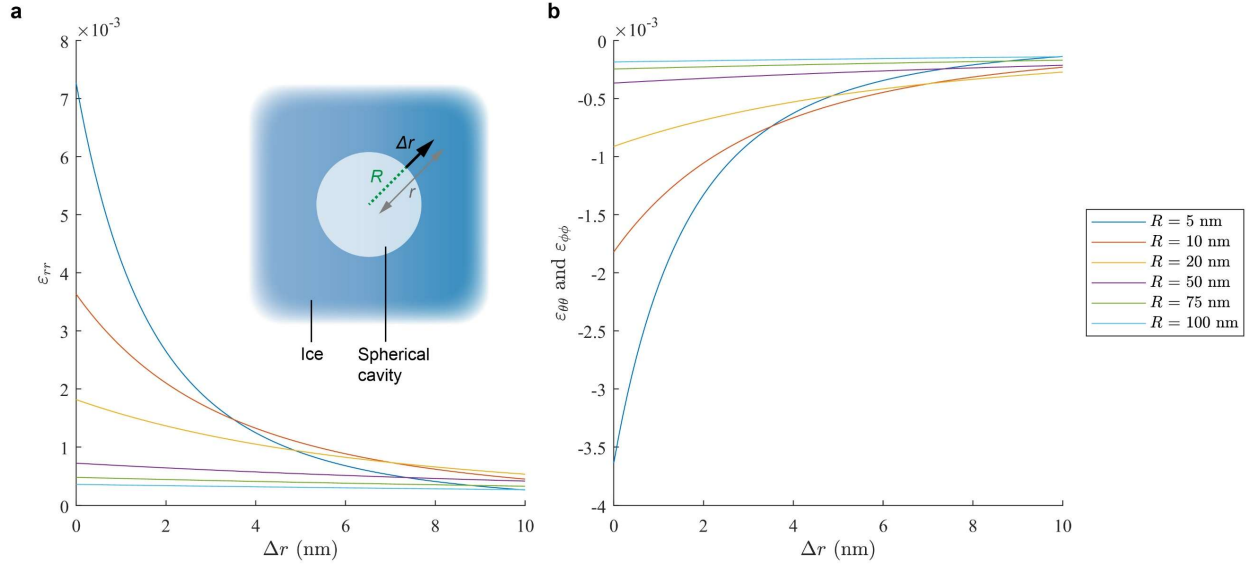
**Supplementary Eq. 10**

Strain components on the surface can be obtained by evaluating it at  $r = R$ :

$$\begin{aligned} \varepsilon_{rr}|_{r=R} &= \frac{p^\emptyset}{E}(2\nu - 1) + \frac{2\gamma}{ER}(1 + \nu), \\ \varepsilon_{\theta\theta}|_{r=R} = \varepsilon_{\phi\phi}|_{r=R} &= \frac{p^\emptyset}{E}(2\nu - 1) - \frac{\gamma}{ER}(1 + \nu). \end{aligned}$$

**Supplementary Eq. 11**

For ice, we take a slightly overestimated surface energy<sup>13,14</sup>  $\gamma = 200 \text{ mJ m}^{-2}$ , Young's Modulus<sup>15</sup>  $E = 11 \text{ GPa}$  at  $-180 \text{ }^\circ\text{C}$ , and Poisson's ratio<sup>16</sup>  $\nu = 0.33$ . The radial and tangential strains in the material as a function of the distance to the cavity surface ( $\Delta r$ ) are plotted in Supplementary Fig. 35. The strain components on the cavity surface are calculated by Supplementary Eq. 11 and given in Supplementary Table 7.



**Supplementary Fig. 35. Elastic strain field around a spherical cavity in ice based on continuum theories. a, Radial elastic strain. b, Tangential elastic strain.  $\Delta r$  is the distance to the cavity surface, i.e.,  $r = R + \Delta r$ .**

**Supplementary Table 7. Elastic strain components on the cavity surface in ice based on continuum theories.**

| $R$ (nm) | $\epsilon_{rr} _{r=R}$ | $\epsilon_{\theta\theta} _{r=R}$ and $\epsilon_{\phi\phi} _{r=R}$ |
|----------|------------------------|---|
| 5        | 0.007270               | -0.00364  |
| 10       | 0.003633               | -0.00182  |
| 20       | 0.001815               | -0.00091  |
| 50       | 0.000724               | -0.00037  |
| 75       | 0.000482               | -0.00025  |
| 100      | 0.000361               | -0.00018  |



### Radiolysis calculation

The temperature-dependent kinetic model assumes that the reaction rates  $k$  follow an Arrhenius behavior given by an activation energy  $E_A$  and an Arrhenius factor  $A$  ( $R$  is the gas constant and  $T$  the temperature)<sup>17</sup>:

$$k = Ae^{\frac{E_A}{RT}}$$

### Supplementary Eq. 12

The included reactions and corresponding values for  $A$  and  $E_A$  are listed in Supplementary Table 8. These parameters were acquired for temperatures between 25 and 100 °C. Consequently, applying these rate constants to lower temperatures is an extrapolation of Supplementary Eq. 12.

**Supplementary Table 8. Chemical reactions used in the kinetic model<sup>17</sup>.** In the Arrhenius factor  $A$ ,  $n$  describes the reaction order.

|    | Reaction   | $A$ (mol <sup>-n+1</sup> L <sup>(n-1)</sup> s <sup>-1</sup> ) | $E_A$ (kJ mol <sup>-1</sup> ) |
|----|--|---|-------------------------------|
| 1  | $H^+ + OH^- \longrightarrow H_2O$                    | $1.88 \times 10^{13}$   | 12.62                         |
| 2  | $H_2O \longrightarrow H^+ + OH^-$                    | $1.70 \times 10^6$  | 62.37                         |
| 3  | $H_2O_2 \longrightarrow H^+ + HO_2^-$                | $4.12 \times 10^6$  | 43.77                         |
| 4  | $H^+ + HO_2^- \longrightarrow H_2O_2$                | $5.59 \times 10^{12}$   | 11.73                         |
| 5  | $H_2O_2 + OH^- \longrightarrow HO_2^- + H_2O$        | $3.66 \times 10^{12}$   | 13.98                         |
| 6  | $HO_2^- + H_2O \longrightarrow H_2O_2 + OH^-$        | $4.54 \times 10^{11}$   | 31.74                         |
| 7  | $e_h^- + H_2O \longrightarrow H + OH^-$              | $5.58 \times 10^6$  | 31.73                         |
| 8  | $H + OH^- \longrightarrow e_h^- + H_2O$              | $8.52 \times 10^{13}$   | 37.36                         |
| 9  | $H \longrightarrow H^+ + e_h^-$                      | $2.84 \times 10^{12}$   | 66.66                         |
| 10 | $H^+ + e_h^- \longrightarrow H$                      | $1.98 \times 10^{12}$   | 11.17                         |
| 11 | $HO_2 \longrightarrow O_2^- + H^+$                   | $2.63 \times 10^8$  | 14.58                         |
| 12 | $O_2^- + H^+ \longrightarrow HO_2$                   | $5.59 \times 10^{12}$   | 11.73                         |
| 13 | $HO_2 + OH^- \longrightarrow O_2^- + H_2O$           | $7.13 \times 10^9$  | 60.93                         |
| 14 | $O_2^- + H_2O \longrightarrow HO_2 + OH^-$           | $3.66 \times 10^{12}$   | 13.98                         |
| 15 | $e_h^- + OH \longrightarrow OH^-$                    | $2.64 \times 10^{12}$   | 10.65                         |
| 16 | $e_h^- + H_2O_2 \longrightarrow OH + OH^-$           | $7.75 \times 10^{12}$   | 15.72                         |
| 17 | $e_h^- + H_2O + O_2^- \longrightarrow HO_2^- + OH^-$ | $4.43 \times 10^{10}$   | 12.98                         |
| 18 | $e_h^- + HO_2 \longrightarrow HO_2^-$                | $2.45 \times 10^{12}$   | 12.98                         |
| 19 | $e_h^- + O_2 \longrightarrow O_2^-$                  | $2.53 \times 10^{12}$   | 11.66                         |
| 20 | $2 e_h^- + 2 H_2O \longrightarrow H_2 + 2 OH^-$      | $1.01 \times 10^{10}$   | 20.74                         |
| 21 | $e_h^- + H + H_2O \longrightarrow H_2 + OH^-$        | $2.06 \times 10^{11}$   | 14.93                         |
| 22 | $H + H_2O \longrightarrow H_2 + OH$                  | $7.39 \times 10^{12}$   | 98.24                         |
| 23 | $2 H \longrightarrow H_2$                            | $2.69 \times 10^{12}$   | 15.51                         |
| 24 | $H + OH \longrightarrow H_2O$                        | $4.19 \times 10^{11}$   | 9.03                          |
| 25 | $H + H_2O_2 \longrightarrow OH + H_2O$               | $1.76 \times 10^{11}$   | 21.01                         |
| 26 | $H + O_2 \longrightarrow HO_2$                       | $9.01 \times 10^{11}$   | 10.52                         |
| 27 | $H + HO_2 \longrightarrow H_2O_2$                    | $5.05 \times 10^{12}$   | 15.09                         |
| 28 | $H + O_2^- \longrightarrow HO_2^-$                   | $5.05 \times 10^{12}$   | 15.09                         |
| 29 | $2 OH \longrightarrow H_2O_2$                        | $9.78 \times 10^{10}$   | 7.48                          |

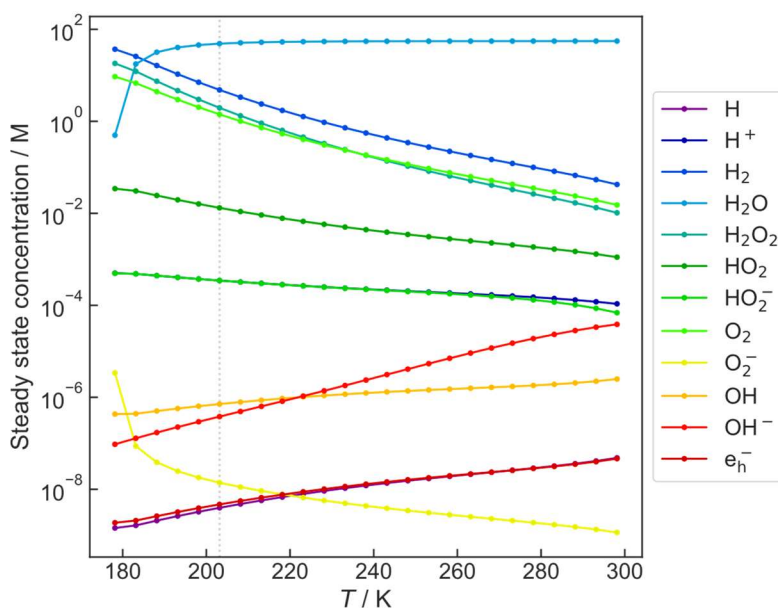
|    |   |                       |       |
|----|---|-----------------------|-------|
| 30 | $\text{OH} + \text{HO}_2 \longrightarrow \text{O}_2 + \text{H}_2\text{O}$           | $1.31 \times 10^{11}$ | 6.68  |
| 31 | $\text{OH} + \text{O}_2^- \longrightarrow \text{OH}^- + \text{O}_2$                 | $8.75 \times 10^{11}$ | 10.84 |
| 32 | $\text{H}_2 + \text{OH} \longrightarrow \text{H} + \text{H}_2\text{O}$              | $6.55 \times 10^{10}$ | 18.45 |
| 33 | $\text{OH} + \text{H}_2\text{O}_2 \longrightarrow \text{HO}_2 + \text{H}_2\text{O}$ | $7.72 \times 10^9$    | 13.82 |
| 34 | $\text{OH} + \text{HO}_2^- \longrightarrow \text{HO}_2 + \text{OH}^-$               | $1.00 \times 10^{12}$ | 11.92 |
| 35 | $\text{HO}_2 + \text{O}_2^- \longrightarrow \text{HO}_2^- + \text{O}_2$             | $2.62 \times 10^9$    | 8.09  |
| 36 | $2 \text{HO}_2 \longrightarrow \text{O}_2 + \text{H}_2\text{O}_2$                   | $2.77 \times 10^9$    | 20.07 |

As the inelastic scattering of high-energy electrons in amorphous ice is close to water<sup>18,19</sup>, room-temperature  $G$ -values are chosen for the simulation (Supplementary Table 9). We note, however, that  $G$ -values are known to change as a function of temperature, which has been approximated linearly<sup>10</sup>. Yet, linear extrapolation was ruled out for cryogenic temperatures, as this would quickly yield physically unreasonable results.

**Supplementary Table 9.  $G$ -values used in this work<sup>20</sup>.**

| Reactant                                | $e_h^-$ | $\text{H}^+$ | $\text{OH}^-$ | $\text{H}$ | $\text{OH}$ | $\text{HO}_2$ | $\text{H}_2$ | $\text{H}_2\text{O}_2$ | $\text{H}_2\text{O}$ |
|---|---------|--------------|---------------|------------|-------------|---------------|--------------|------------------------|----------------------|
| $G_i$ ( $10^{-2}$ Molecules $eV^{-1}$ ) | 2.60    | 3.10         | 0.50          | 0.66       | 2.70        | 0.02          | 0.45         | 0.70                   | -4.64                |

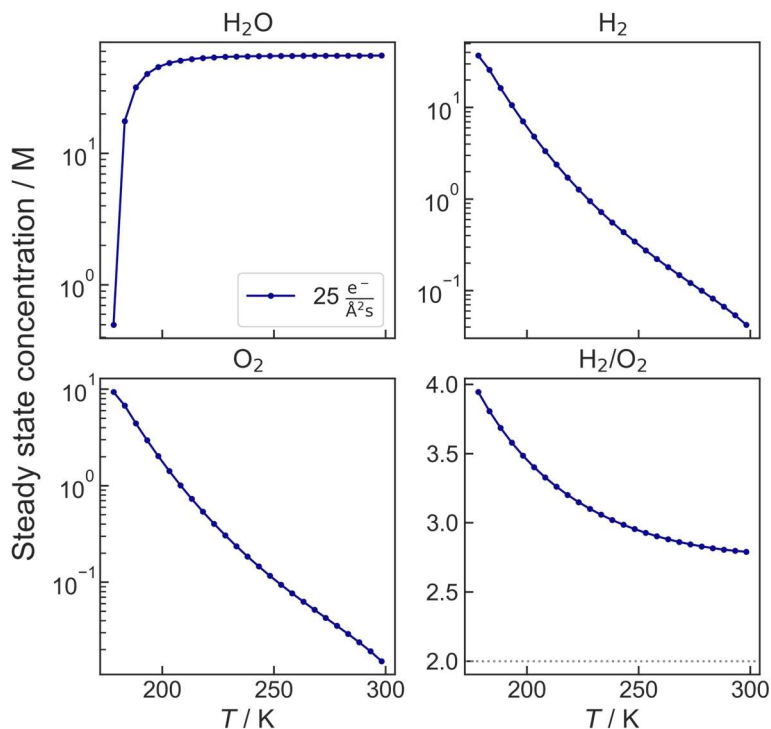
All simulations based on Eq. 1 (Methods section) were conducted for 1000 s, sufficient to ensure steady state formation for all reactants. The evolution of chemical species under the experimental conditions of in situ bubble generation is given in Fig. 5f. The steady state at different temperatures at an electron flux of  $25 \text{ e } \text{\AA}^{-2} \text{ s}^{-1}$  is given in Supplementary Fig. 36.



**Supplementary Fig. 36. Radiolysis steady states as a function of temperature ( $T$ ).** The dotted vertical line denotes the temperature of in situ bubble generation in this work.

The steady-state concentrations of the stable main products of water radiolysis ( $\text{H}_2$ ,  $\text{O}_2$ ,  $\text{H}_2\text{O}_2$ ) increase with cooling (Supplementary Fig. 37). Similarly, the ratio between  $\text{H}_2$  and  $\text{O}_2$ , presumably the dominant

gas species, also increases with temperature reduction. Consequently, mass balance eventually causes substantial water depletion. Here, the computation of the kinetic model fails because the physicochemical principles behind the model assume the primary interaction of electrons with water. If water depletes, the used  $G$ -values break down. In the present case, steady states were successfully simulated down to about 180 K. We note that this does not necessarily mean that at lower  $T$ , no steady state is expected; however, a model considering irradiation of  $\text{H}_2\text{O}$  alone is not feasible to describe the system accurately.



**Supplementary Fig. 37. Steady-state concentrations of water and main gas components from radiolysis calculations as a function of temperature ( $T$ ).** The molar ratio between  $\text{H}_2$  and  $\text{O}_2$  increases with temperature reduction.

Noteworthy is the increase in the steady-state concentration of  $\text{O}_2$  with reduced temperature, which is in good agreement with EELS measurements in cryo-TEM<sup>21</sup>. This indicates that the model is feasible for drawing qualitative conclusions despite the discussed approximations and limitations.

## Captions for Supplementary Movies

**Supplementary Movie 1.** Focal-series HRTEM images of a through-hole in thin ice films (left) and corresponding Fourier transform (right).

**Supplementary Movie 2.** Time-sequence HRTEM images (left), lowpass-filtered HRTEM images (middle), and Fourier transform (right) of bubble nucleation and growth.

**Supplementary Movie 3.** Time-sequence HRTEM images (left), lowpass-filtered HRTEM images (middle), and Fourier transform (right) of bubble dissolution.

**Supplementary Movie 4.** Time-sequence HRTEM images (left), lowpass-filtered HRTEM images (middle), and Fourier transform (right) of bubble coalescence.

## Descriptions of Other Supplementary Datasets

**Supplementary Data 1.** Models from MD simulations of ice grain boundaries with various tilt angles and thicknesses. Format: coordinate files, xyz.

**Supplementary Data 2.** Models from MD simulations of ice cavities. Format: coordinate files, xyz.

**Supplementary Data 3.** Temperature-dependent concentration evolution of chemical species from radiolysis calculations. Format: Microsoft Excel worksheets, xlsx.

## References

- 1 Morgan, D. J. Comments on the XPS Analysis of Carbon Materials. *C-J. Carbon Res.* **7**, 51, (2021).
- 2 Stalder, A. F. *et al.* Low-bond axisymmetric drop shape analysis for surface tension and contact angle measurements of sessile drops. *Colloids Surf. A* **364**, 72-81, (2010).
- 3 Prydatko, A. V., Belyaeva, L. A., Jiang, L., Lima, L. M. C. & Schneider, G. F. Contact angle measurement of free-standing square-millimeter single-layer graphene. *Nat. Commun.* **9**, 4185, (2018).
- 4 Fraundorf, P., Qin, W., Moeck, P. & Mandell, E. Making sense of nanocrystal lattice fringes. *J. Appl. Phys.* **98**, 114308, (2005).
- 5 Mallick, S. P., Carragher, B., Potter, C. S. & Kriegman, D. J. ACE: Automated CTF Estimation. *Ultramicroscopy* **104**, 8-29, (2005).
- 6 Chan, H. *et al.* Machine learning coarse grained models for water. *Nat. Commun.* **10**, 379, (2019).
- 7 Shewchuk, J. R. An introduction to the conjugate gradient method without the agonizing pain. (Carnegie Mellon University, 1994).
- 8 Thompson, A. P. *et al.* LAMMPS—a flexible simulation tool for particle-based materials modeling at the atomic, meso, and continuum scales. *Comput. Phys. Commun.* **271**, 108171, (2022).
- 9 Arun, K. S., Huang, T. S. & Blostein, S. D. Least-squares fitting of two 3-D point sets. *IEEE Trans. Pattern Anal. Mach. Intell.* **PAMI-9**, 698-700, (1987).
- 10 Ong, S. P. *et al.* Python Materials Genomics (pymatgen): A robust, open-source python library for materials analysis. *Comput. Mater. Sci.* **68**, 314-319, (2013).
- 11 Togo, A., Shinohara, K. & Tanaka, I. Spglib: a software library for crystal symmetry search. arXiv:1808.01590 (2018). <<https://arxiv.org/abs/1808.01590>>.
- 12 Landau, L. D., Lifshitz, E. M., Kosevich, A. M. & Pitaevskii, L. P. in *Theory of Elasticity* Vol. 7 *Course of Theoretical Physics* Ch. 1, 1-37 (Butterworth-Heinemann, 1986).
- 13 Douillard, J. M. & Henry, M. Calculation of surface enthalpy of solids from an ab initio electronegativity based model: case of ice. *J. Colloid Interface Sci.* **263**, 554-561, (2003).
- 14 Pan, D. *et al.* Surface energy and surface proton order of the ice Ih basal and prism surfaces. *J. Phys.: Condens. Matter* **22**, 074209, (2010).

- 15 Wei, P., Zhuang, D., Zheng, Y.-Y., Zaoui, A. & Ma, W. Temperature and pressure effect on tensile behavior of ice-Ih under low strain rate: A molecular dynamics study. *J. Mol. Liq.* **355**, 118945, (2022).
- 16 Sinha, N. K. in *Sixth International Offshore Mechanics and Arctic Engineering Symposium* Vol. 4 189-195 (Houston, Texas, USA, 1987).
- 17 Ambrožič, B. *et al.* Controlling the radical-induced redox chemistry inside a liquid-cell TEM. *Chem. Sci.* **10**, 8735-8743, (2019).
- 18 Pimblott, S. M., LaVerne, J. A., Mozumder, A. & Green, N. J. B. Structure of electron tracks in water. 1. Distribution of energy deposition events. *J. Phys. Chem.* **94**, 488-495, (1990).
- 19 Yesibolati, M. N. *et al.* Electron inelastic mean free path in water. *Nanoscale* **12**, 20649-20657, (2020).
- 20 Pastina, B. & LaVerne, J. A. Effect of Molecular Hydrogen on Hydrogen Peroxide in Water Radiolysis. *J. Phys. Chem. A* **105**, 9316-9322, (2001).
- 21 Abellan, P., Gautron, E. & LaVerne, J. A. Radiolysis of Thin Water Ice in Electron Microscopy. *J. Phys. Chem. C* **127**, 15336-15345, (2023).